Scalable human neuronal models of tauopathy producing endogenous seed-competent 4R tau

Eliona Tsefou[1,*], Sumi Bez[1], Timothy J.Y. Birkle[1], Martha Foiani[1], Naoto Watamura[1], Mathieu Bourdenx[1], Daria Gavriouchkina[1], Emir Turkes[1], Samuel Crawford[2], Rachel Coneys[1,2], Adrian M. Isaacs[1,2], Karen Duff[1,*].

[1]UK Dementia Research Institute, University College London, London, UK

[2]Department of Neurodegenerative Disease, UCL Queen Square Institute of Neurology, London, UK

*Correspondence: e.tsefou@ucl.ac.uk or k.duff@ucl.ac.uk

Abstract

Pathological accumulation of four-repeat (4R) tau is central to several frontotemporal dementia (FTD) subtypes but human neuronal models amenable to high-throughput screening of 4R tau-targeting therapies remain limited. To address this, we developed iPSC-derived i^{3}Neuron (i^{3}N) lines expressing >75% 4R tau, driven by FTD splice-shifting mutations (S305N or S305N/IVS10+3). These neurons develop hyperphosphorylated tau and demonstrate somatodendritic mis-localisation. Unlike other stem cell models of tauopathy, these i^{3}N neurons develop endogenous seed-competent tau and present pFTAA-positive tau assemblies after 28 days in culture. For scalable screening, we CRISPR-engineered a HiBiT luminescence tag at the endogenous *MAPT* locus into the S305N/IVS10+3 iPSC line, enabling precise quantification of tau levels and pharmacological responses. The model responded predictably to compounds affecting tau clearance, demonstrating its suitability for drug discovery. Overall, this i^{3}N platform recapitulates key features of 4R tauopathy and provides a robust system to identify therapeutic modulators of pathological tau.

Introduction

Tauopathies are a heterogeneous group of neurodegenerative disorders defined by the accumulation of pathological forms of the microtubule-associated protein tau (MAPT) in the brain. These include progressive supranuclear palsy (PSP), corticobasal degeneration (CBD), Pick's disease, and frontotemporal dementia with Parkinsonism linked to chromosome 17 (FTDP-17)[1]. In these diseases, tau aggregates into intracellular fibrils that interfere with neuronal function and viability[2,3]. Tau exists in six isoforms in the adult human brain, produced by alternative splicing of exons 2, 3, and 10 of the *MAPT* gene[4]. These isoforms differ in the number of N-terminal inserts and in the presence of either three (3R) or four (4R) microtubule-binding repeats[5]. During foetal development, the human brain predominantly expresses 3R tau,[6] but in the healthy adult brain, the ratio of 3R:4R tau is balanced[7-9]. Disruption of this balance, particularly an excess of 4R tau, is strongly associated with several tauopathies[10,11].

Human induced pluripotent stem cell (iPSC)-derived neurons are a valuable tool to study early mechanisms of neurodegenerative diseases. However, using such human neuronal models to recapitulate 4R tau expression has historically been difficult as they typically express predominantly 0N3R tau, reflecting foetal-like tau splicing[12-16]. Until recently, most of the iPSC-derived neuronal models that were able to induce moderate expression of 4R tau required prolonged and complicated culturing conditions to achieve a moderate increase in 4R tau expression or they relied on the insertion of multiple tau mutations[17-21]. An alternative neuronal model involves direct conversion of fibroblasts

into induced neurons (miNs), which bypass the pluripotent state and retain age-associated epigenetic features[22]. We showed that miNs robustly express adult tau isoforms (including 4R tau) and they developed seed-competent aggregated tau[22]. While direct conversion allows for the preservation of donor-related age and disease state, they are not suitable for drug discovery as: (i) availability of patient derived fibroblasts is limited; (ii) they cannot be maintained in culture indefinitely; (iii) the yield of neurons is typically low; (iv) and there are significant challenges in batch reproducibility.

The S305N mutation, located at the end of exon 10, causes excessive production of 4R tau and consequently leads to FTLD-MAPT[23-25]. Postmortem brain tissue from S305N carriers exhibit 4R tau-positive inclusions, including neurofibrillary tangles and ring-like structures surrounding neuronal nuclei, reflecting severe tau pathology [26,27]. A recent study has shown that an isogenic set of iPSC lines derived from a S305N mutation carrier presents increased expression of 4R tau after a few months in culture[28]. In the current study, we employ an i^3Neuronal (i^3N) version of the same isogenic S305N iPSC lines, as well as a novel CRISPR-Cas9-edited iPSC line where we introduced the S305N point mutation and the IVS10+3 intronic mutation to further enhance 4R levels. The IVS10+3 mutation is spliced out of the mature mRNA and the resulting protein only expresses the single mutation, at S305N. Elevated 4R tau resulted in tau hyperphosphorylation, changes in the cytoskeleton and, remarkably, endogenous seed-competent tau. Endogenous tau seeds have not been reported for other iPSC-derived FTLD-MAPT lines. We have tested this line with tau-modulating drugs, and we anticipate it can be developed into a platform for drug testing. In summary, we have developed a novel human neuron model that recapitulates key aspects of FTLD-MAPT that can be used to identify key pathogenic mechanisms as well as to test potential therapeutics for tauopathies. Although the lines express an FTLD-MAPT associated mutation, they recapitulate many key features observed in Alzheimer's disease and they are therefore a suitable model for drug screening targeting tau in a range of neurodegenerative diseases.

Results

i^3N neurons with an S305N mutation predominantly express 4R tau after 7 days of differentiation.

It is well established that iPSC-derived neurons predominantly express the 3R isoform of tau [13-16]. Most of the existing iPSC-derived neuronal models capable of generating 4R tau rely on the introduction of multiple mutations (>3) to drive this shift[20,21]. Building on insights from a targeted mouse model where combining both S305N and IVS10+3 FTLD-MAPT-related mutations led to the expression of 99% 4R MAPT[29], we aimed to determine whether a similar shift could be achieved in an iPSC-derived neuronal model. The S305N mutation affects the RNA stem-loop structure that regulates alternative splicing of exon 10 in the *MAPT* gene[30]. The intronic IVS10+3 mutation lies adjacent to the splice-donor site and also disrupts the stem-loop structure of the pre-mRNA, promoting increased exon 10 inclusion[31,32].

To generate our model, we used a commercially available iPSC line from Synthego (802:30F; referred to as WT) and introduced the mutations using CRISPR-Cas9 with a single guide RNA (Figure S1A). As the IVS10+3 mutation is spliced out, only a single, FTLD-MAPT-causing mutation is present in the protein and the cells are therefore a valid model of human 4R tauopathy. Two edited, homozygous clones, S305N_C1 and S305N_C2, were isolated and used for experiments. In addition to these lines, we used a patient-derived S305N heterozygous line (isoHet S305N), along with isogenic wild-type (isoWT) and homozygous (isoHom S305N) lines (available from NCRAD, Bowles *et al.* Figure 1A)[28]. All iPSC lines were transfected with a doxycycline-inducible human *Neurogenin-2* (hNGN2) transgene using the piggyBac transposon system (Figure 1A)[33]. Stable integration of hNGN2 enabled rapid differentiation into excitatory human cortical glutamatergic neurons (i^3Ns) within three days of

doxycycline exposure. Post-transfection, all lines maintained normal karyotypes (assessed via low-coverage whole genome sequencing) and continued to express pluripotency markers (Figure S1B–E).

To assess the effect of the mutations on exon 10 inclusion, we differentiated all WT and mutant iPSC lines into i^3N neurons using a two-step protocol adapted from Fernandopulle *et al.*[34], culturing them for up to 28 days. We examined MAPT isoform expression by semi-quantitative PCR (semi-qPCR), focusing on the inclusion (4R MAPT) or exclusion (3R MAPT) of exon 10 (Figure 1B). As expected, both WT and isoWT lines exclusively expressed 3R tau throughout differentiation (DIV7–DIV28). In contrast, both S305N_C1 and C2 clones expressed >80% 4R tau as early as DIV7, increasing to >90% by DIV28. The isoHet S305N line exhibited a 3R:4R ratio of approximately 60:40 at DIV7, shifting to a nearly 50:50 ratio by DIV28 which is consistent with ratios observed in the healthy adult human brain[7-9]. The isoHom S305N line started with 55:45% 3R:4R tau at DIV7 which reached ~25:75% 3R:4R by DIV28 indicating significantly lower 4R levels compared to the S305N_C1 and C2 clones (Figure 1C, D). The level of total *MAPT* RNA was quantified by RT-qPCR and no change was observed (Figure 1E). MAPT mRNA could not be detected in the neuronal lines before DIV7.

Characterization of S305N i^3N neurons

To assess the effects of the S305N mutation and 4R tau elevation on neuronal maturation, we analysed neuronal marker expression at DIV21 and DIV28 by immunocytochemistry. All i^3N neuronal lines were stained for βIII-tubulin (TUJ1) (an axonal marker), MAP2 (a somatodendritic marker) and NeuN, a nuclear marker associated with neuronal maturity (Figure 1F). No difference in TUJ1 expression was observed between S305N_C1 and C2 and the WT control at either timepoint (Figure S2A). In the isoHet and isoHom S305N lines, TUJ1 expression remained comparable to the isoWT control (Figure S2B). While overall TUJ1 expression was unchanged, we noted the emergence of irregular, swollen axonal protrusions in all lines carrying the S305N mutation, particularly at DIV28. These structures may represent axonal blebbing, which is commonly associated with neuronal stress, injury, or degeneration[35,36]. MAP2 mRNA levels did not differ between lines but increased over time in all neuronal cultures, reaching a plateau after DIV21 (Figure 1G). However, the level of MAP2 protein was significantly reduced in both S305N_C1 and C2 neurons (Figure 1H), whereas no change was detected in the isoHet and isoHom S305N lines (Figure 1I). The observed reduction in MAP2 protein in the S305N_C1 and C2 lines may point to cytoskeletal instability, which coincides with the tubulin blebbing in these neurons. NeuN staining revealed that over 80% of cells in all lines were NeuN-positive, indicating a high proportion of mature neurons (Figure S1C).

We also examined the expression of VGLUT1, a marker of glutamatergic synapses. VGLUT1 mRNA levels decreased over time, reaching a plateau around DIV17 (Figure S2D). At the protein level, immunocytochemistry at DIV21 and DIV28 revealed a statistically significant reduction in VGLUT1 expression in the S305N_C1 and C2 lines, with C1 showing nearly a 50% decrease compared to WT (Figure S2E and F). In contrast, no difference was observed in the isoHet and isoHom S305N lines (Figure S2G). Reduced VGLUT1 expression may indicate synaptic dysregulation in the S305N_C1 and C2 lines, consistent with observations from the mouse model expressing the same mutations, which exhibited synaptic loss[29]. Both S305N_C1 and C2 presented similar changes; however, for some measurements (*e.g.*, blebbing or MAP2 levels), a stronger phenotype was evident in the S305N_C1 neurons. We therefore decided to focus on clone C1 for further experiments.

Mis-localization and distribution of tau in neurons expressing S305N mutant isoforms

Tau undergoes proteolytic cleavage by various proteases, generating fragments that contribute to the pathogenesis of several neurodegenerative disorders[37,38]. To investigate the subcellular distribution of

tau, we performed immunocytochemistry on methanol-fixed neurons at DIV21 and DIV28 using antibodies targeting distinct tau domains: Tau13 (N-terminus, epitope 2–18 aa), HT7 (mid-region, epitope 159–162 aa), and TauC (C-terminus, epitope 244–441 aa) (Figure 2A). In both WT and isoWT neurons, Tau13 and TauC labelled tau both in the somatodendritic compartment (co-localized with MAP2, Figure 2B) and in the axons (Figure S3A, co-localized with TUJ1), with signal intensity increasing between DIV21 and DIV28 (Figure 2B). Notably, HT7 exhibited a prominent perinuclear signal, particularly in WT cells. In contrast, S305N_C1 neurons displayed pronounced somatodendritic tau retention with markedly reduced axonal staining (Figure 2B and Figure S3A). Densitometric analysis revealed an >80% reduction in total tau signal detected by all three antibodies in this group (Figure 2C, E, G). In the isoHet and isoHom S305N mutant neurons, tau remained detectable in both the somatodendritic compartment and axons (Figure 2B and Figure S3A). Among the antibodies, Tau13 showed the least variability and revealed significantly reduced tau levels in isoHet neurons at DIV28, with a trend toward reduction observed in isoHom neurons (22% reduction, $p = 0.0894$). Interestingly, HT7 was the only antibody that detected significantly increased tau levels in isoHom neurons at DIV28 ($p = 0.0152$). Since HT7 targets a mid-region tau epitope, this selective increase suggests the accumulation of tau fragments retaining the mid-region but lacking either the N- or C-terminal epitopes, possibly due to aberrant proteolysis.

Furthermore, neurons expressing isoHet and isoHom S305N tau displayed distinct tau-positive "blebs" at DIV28 when stained with Tau13 and TauC (Figure 2B, arrows). Co-staining with TUJ1 revealed partial colocalization of these tau "blebs" with tubulin-rich structures (Figure S3A, arrows). Overall, these results suggest that homozygote S305N mutations or high levels of 4R tau led to both mislocalization and altered levels of tau, particularly affecting its axonal distribution. The most profound changes were observed in S305N_C1 neurons, where tau was almost exclusively confined to the somatodendritic compartment. While tau remained detectable in axons of isoHet and isoHom neurons, overall levels trended lower, especially as revealed by Tau13 and TauC staining.

Increased tau phosphorylation depending on S305N isoform

To investigate the effects of the S305N mutation on tau phosphorylation, we examined the expression and distribution of phospho-tau (pTau) epitopes using the following antibodies: AT8 (pSer202/pThr205), CP13 (pSer202) and AT100 (pThr212/pSer214). Immunocytochemistry was performed on methanol-fixed neurons at DIV21 and DIV28 (Figure 3A). In S305N_C1 neurons, AT8 staining was predominantly localized to the somatodendritic compartment, whereas in the WT neurons AT8 staining was much lower (Figure 3B). Quantitative analysis revealed a significant increase in AT8 signal at DIV21 ($p = 0.0083$), whereas at DIV28 AT8 levels did not change between WT and S305N_C1 (Figure 3C). When normalizing AT8 levels to total tau (via TauC) we observed a significant increase at both timepoints, despite the overall reduction in total tau levels in this line (Figure S3C; AT8/TauC staining not shown). CP13 staining in S305N_C1 neurons showed both somatodendritic and axonal localization. However, total CP13 signal was significantly reduced compared to WT (Figure 3D). After normalization to TauC, a trend toward increased CP13 levels was observed at DIV28 (Figure S3B and D). Surprisingly, AT100 staining in S305N_C1 neurons was restricted exclusively to the axons (Figure 3B). Given the overall reduction in total tau in this line, the presence of detectable AT100 signal suggests extremely low levels of tau were still localized within the axonal compartment. Interestingly, AT100 diverged between genotypes: while signal decreased over time in WT neurons, it progressively increased in S305N_C1 neurons (Figure 3E).

In isoHet and isoHom S305N neurons, AT8 and CP13 signal was evident in both soma and axons. Levels increased in a dose-dependent manner relative to S305N allele copy number compared to their

isogenic WT controls at DIV21 (Figure 3B, F, G). At DIV28, both AT8 and CP13 levels were significantly elevated in isoHet and isoHom neurons. AT100 in the isoWT neurons mirrored the trend seen in WT neurons, showing a reduction over time. In isoHet neurons, the level of AT100 significantly increased at DIV28 (p=0.0005), whereas in isoHom neurons, elevated AT100 signal was detected at both timepoints (Figure 3H). Notably, unlike AT8 and CP13, AT100 did not exhibit a clear allele-dose-dependent increase.

Collectively, these results highlight distinct phosphorylation patterns and subcellular localization profiles of tau in neurons with elevated 4R tau, expressing the S305N mutation. Some phospho-epitopes, such as AT8, were restricted to the soma (e.g., in S305N_C1), others were distributed in both soma and axons (e.g., CP13), while AT100 was found exclusively in axons. These patterns may reflect the interplay between isoform composition, total tau levels and subcellular localization of tau. Increased 4R tau in S305N mutant neurons influenced both isoform composition, the phosphorylation status and the spatial distribution of tau proteoforms.

Temporal analysis of total and phosphorylated tau reveals early alterations in S305N mutant neurons

To determine whether the observed reduction in total tau levels in S305N_C1 neurons at DIV21 and DIV28 represents an early developmental event or a progressive consequence of differentiation, we performed immunoblotting on lysates collected from DIV7 to DIV28. Blots were probed with antibodies against total tau (Tau13, HT7, TauC) and phosphorylated tau (pTau) (CP13, AT8; Figure 4A). Across all timepoints, S305N_C1 neurons displayed consistently lower levels of total tau compared to WT controls (Figure S4A, B and C). As previous studies focused on DIV21 and DIV28, we specifically compared tau expression at these timepoints, as well as at DIV10, the earliest timepoint where tau was detected with all antibodies used. At all-time points, significant reductions in tau were observed using all total tau antibodies in S305N_C1 neurons compared to the WT control (Figure 4B, C Figure S4H, I, J). Tau protein expression in both WT and S305N_C1 neurons increased over time, mirroring MAPT mRNA expression patterns; however, at no timepoint did tau levels in S305N_C1 neurons reach those observed in WT neurons. In the isoHet S305N neurons, both Tau13 and TauC, but not HT7, were significantly increased at DIV10 (Figure 4B left graphs, Figure S4H), but no significant changes were observed at DIV21 and DIV28 compared to isoWT (Figure 4B and C, Figure S4I and J). A trend toward reduced Tau13 levels in the isoHet neurons was observed, though it did not reach significance. In the isoHom S305N neurons, a ~40% reduction in Tau13 was observed at DIV21 and DIV28, while TauC and HT7 showed a trend toward reduced levels (~20% reduction, Figure 4B, C and Figure S4H, I and J; Graphs on the left). Notably, Tau13 and TauC changes mirrored immunocytochemistry results, except for HT7, where an increase was observed at DIV28 in the isoHom S305N neurons. This could potentially reflect methodological differences between immunoblotting and immunocytochemistry. A trend towards reduced total tau levels in the same lines was also observed by Bowels e*t al.* when using the direct differentiation approach to generate cortical neurons[28]. Generally, the reduction in total tau levels seems to occur only in neurons expressing more than 70% 4R MAPT/tau.

Phosphorylated tau levels showed a similar pattern to tau in the S305N_C1 neurons over time (Figure S5D-F). CP13 and AT8 expression were significantly reduced in S305N_C1 neurons when normalized to total protein at DIV10, 21 and 28 (Figure S4H, I and J graphs in middle and right). When normalized to TauC, the reduction in CP13 was attenuated and a trend toward increased levels was observed at DIV10 and 21, which became statistically significant at DIV28 in the S305N_C1 compared to WT neurons (Figure 4D and E). Interestingly, the ratio of AT8/TauC was elevated at earlier timepoints (DIV10), but declined thereafter, suggesting an early burst of phosphorylation at pSer202/pThr205

(Figure 4E). It is important to note that, based on immunocytochemistry, AT8/TauC levels were increased, possibly due to differences in detecting phosphorylated epitopes between techniques, which can affect accessibility. Elevated CP13 levels normalized to total tau indicate tau hyperphosphorylation in S305N_C1 neurons.

Consistent with staining data, both CP13 and AT8 levels were elevated in isoHet and isoHom neurons over time (Figure S5D-G). When normalized to total protein, CP13 expression increased in the isoHet S305N relative to isogenic WT controls at DIV10 and DIV21, but it did not reach significance at DIV28 (Figure S4H, I and J graphs in the middle). In the isoHom S305N, CP13 levels were also increased by >40% at DIV28; however, this did not reach significance (Figure S4H, I and J graphs in the middle). Notably, at DIV28, a 4R MAPT-dependent increase in CP13 levels was observed (Figure S4J, graph in the middle). AT8 levels followed a similar pattern but did not reach significance at any timepoint due to variability (Figure S4H, I and J graphs on the right). Both CP13 and AT8 were also normalised to total tau. CP13/TauC was statistically significantly increased in isoHom S305N neurons at DIV10 and DIV28 and presented a trend towards increase expression in the isoHet S305N compared to isoWT neurons (Figure 4D). Similarly, when we normalized AT8 levels to TauC a significant increase in AT8 levels was observed in the isoHom S305N compared to isoWT neurons at DIV10 and DIV21 (Figure 4E). AT8/TauC levels were increased in the isoHet S305N, but that change was only significant at DIV28 (Figure 4E). A 4R MAPT-dependent increase in AT8/TauC levels was also noted at DIV10 and DIV21 (Figure 4E,). The increase in CP13/TauC and AT8/TauC indicated that tau is hyperphosphorylated in the isoHet and isoHom S305N neurons. Notably, both AT8 and CP13 signals were detectable as early as DIV7 in both neuronal lines, indicating early tau phosphorylation in these lines (Figure 4A red arrows and Figure S4K).

To further characterize the isoform composition of tau in each neuronal genotype, protein samples were dephosphorylated and analysed by Western blot with Tau13 immunolabelling. As expected, WT and isoWT neurons expressed predominantly 0N3R tau at DIV21 and DIV28, consistent with tau splicing profiles in iPSC-derived neurons (Figure S4M). In contrast, S305N_C1 neurons expressed only 0N4R tau across both timepoints. IsoHet neurons exhibited a 1:1 ratio of 0N3R to 0N4R tau, while isoHom neurons expressed around 58% 0N4R tau at DIV28.

These findings confirm that S305N_C1 neurons consistently express only 4R tau during differentiation and fail to reach WT-equivalent total tau levels. Although isoHet and isoHom neurons also showed reduced total tau after DIV21, both lines exhibited substantial phosphorylated tau accumulation early in development. This early, and 4R MAPT-dependent phosphorylation of tau, particularly in the context of elevated 4R tau, may underlie the pathophysiological changes associated with mutations that increase exon 10 inclusion, as we have seen in post-mortem human tissue[24,26,27,39,40].

S305N mutant neurons develop endogenous tau oligomers and seeds

To evaluate the aggregation potential of tau in S305N mutant neurons, we performed immunocytochemistry using the tau oligomer-recognizing antibody TOC1 developed by Lester Binder's lab[41], on methanol-fixed cells at DIV21 and DIV28. Neurons were co-stained with MAP2 and TUJ1 to assess subcellular localisation. At DIV28, TOC1 signal was undetectable in WT and isoWT neurons; in contrast, neurons harbouring the S305N mutation exhibited markedly increased TOC1 staining (Figure 5A). In S305N_C1 neurons, TOC1 signal was predominantly perinuclear and strongly colocalised with MAP2 (see enlarged MAP2/TOC1 panels). Notably, there was minimal colocalization with TUJ1 or tubulin "blebs" in these neurons. Both isoHet and isoHom S305N neurons also displayed elevated TOC1 staining at DIV28, with isoHet neurons appearing to exhibit slightly higher levels. In these cells, TOC1 occupied a significant portion of the MAP2-positive area, with occasional puncta

extending into TUJ1-positive regions. In some cases, these puncta colocalised with tubulin blebs (TUJ1/MAP2/TOC1 panels, arrows). Quantitative analysis confirmed a significant increase in TOC1 signal in all S305N-mutant neurons compared to their isogenic WT controls at DIV28 (Figure 5B). At DIV21, TOC1 signal was also detectable and largely restricted to MAP2-positive somatodendritic compartments (Figure S5A). Colocalization of TOC1 with tubulin blebs was again observed in isoHom neurons (Figure S5B). Statistically significant increases in TOC1 signal were found in S305N_C1 and isoHet neurons at this earlier timepoint. To confirm that TOC1-positive puncta reflected accumulated tau, we performed co-staining with Tau13. Colocalization between TOC1 and Tau13 was observed in DIV28 neurons, supporting the specificity of TOC1 for tau species (Figure S5C).

To assess whether S305N neurons developed tau seeds, we performed a modified seeding assay[42] using a tau biosensor cell line expressing the repeat domain of tau with the S305N mutation fused to YFP (S305N biosensor[29]). TBS-soluble extracts from DIV28 S305N_C1, isoHet, and isoHom neurons triggered a significant increase in tau inclusion formation compared to their respective isogenic WT controls (Figure 5C, D). In contrast, extracts from DIV21 neurons did not induce seeding activity (Figure S5E), suggesting that seed-competent tau develops later in neuronal maturation. Collectively, these results indicate that S305N mutant neurons develop robust TOC1-positive assemblies, and seed-competent tau species capable of propagating aggregation in a cellular biosensor model.

Post-mortem human frontal cortex brain tissue from an S305N mutation carrier demonstrated tau pathology consistent with our findings in i^3N neurons. Neurons in the human S305N case were positive for AT8, CP13, TOC1 and MC1 (Figure 5E). Ring-shaped tau aggregates surrounding neuronal nuclei were visualised using TOC1 and MC1 antibodies. These observations are consistent with previously reported pathological features identified in human S305N FTLD-MAPT tissue. [24,26,27,29,39,40,43]. TBS-soluble extract from S305N human brain tissue was able to template the aggregation of tau in the S305N biosensor line (Figure 5F). Overall, our S305N i^3N neurons recapitulate key aspects of human pathology with the exception of MC1 immunoreactivity. Given the short culture times, these cells may therefore reflect the earliest tau-related pathological changes observed in humans.

Live imaging reveals progressive accumulation of tau assemblies in S305N neurons

Seeding assays indicated that neurons carrying the S305N mutation develop seed-competent tau by DIV28, but not at DIV21. Given that TOC1-positive signal was detected at both timepoints, we next sought to monitor the longitudinal formation and progression of tau assemblies in live neurons. To accomplish this, we used the conformation-sensitive fluorescent dye pentameric formyl thiophene acetic acid (pFTAA), which selectively binds to β-sheet-rich protein aggregates, including both early tau oligomers and mature fibrils[44,45]. Previous studies have shown that pFTAA is non-toxic and remains stable in primary neuronal cultures for extended periods with routine media replacement[45]. pFTAA and a far-red live tubulin dye were applied to neurons at DIV25, and the accumulation of tau assemblies was imaged over a 72-hour period (Figure 6A). In S305N_C1 neurons, pFTAA-positive puncta were first observed within axonal processes, identified by tubulin staining. Over time, larger aggregates formed, predominantly pre-axonal segments or in proximity to the nucleus (arrows in enlarged panel, Figure 6A). Quantification revealed that pFTAA-positive puncta began to emerge approximately 18 hours after dye application and progressively increased over time in the S305N_C1 neurons (Figure 6B). In contrast, isoHet and isoHom S305N neurons showed pFTAA accumulation as early as 30 minutes after incubation (DIV25), indicating a more rapid onset of aggregate formation or that aggregates are already present (Figure 6A). Some pFTAA-positive areas appeared in regions formerly occupied by viable neurons, while others extended from pre-existing pFTAA accumulations. These puncta were consistently observed in tubulin-rich regions and along axon-like projections (Figure 6A,

arrows). Quantitative analysis confirmed a steady increase in pFTAA signal in both isoHet and isoHom S305N neurons throughout the imaging period (Figure 6C). WT and isoWT neurons, in contrast, exhibited very little pFTAA signal at all timepoints.

As pFTAA is not specific for tau, we confirmed that the pFTAA signal seen in the S305N cells represented tau assemblies by co-staining methanol-fixed neurons with TauC (total tau) and TOC1 (oligomeric tau). In all S305N-mutant lines, pFTAA signal colocalised with TauC, and it was predominantly perinuclear (Figure 6D). As both TOC1 and pFTAA can stain dying neurons, we co-stained with MAP2 to assess neuronal viability. Most pFTAA- and TOC1-positive neurons also stained positively for MAP2, suggesting they were still viable and part of the neuronal cell population (Figure 6E). Further, colocalization of pFTAA with Lysotracker Red in S305N_C1 neurons revealed that tau assemblies were accumulating in lysosomes, rather than being degraded at DIV28 (Figure S7A). These results demonstrate that tau assemblies in S305N neurons develop progressively over time, with isoHet and isoHom neurons exhibiting earlier and more extensive aggregate formation than S305N_C1. The pFTAA-positive structures likely represent early oligomeric and potentially protofibrillar tau species that accumulate in tubulin-rich compartments and evade lysosomal degradation, contributing to the pathogenesis of tauopathy in S305N mutant neurons.

Cytoskeletal alterations in S305N neurons

Tau isoform balance is critical for proper neuronal development, with both 3R and 4R tau contributing to axonogenesis and microtubule stability. S305N_C1 neurons express only 4R tau, and at significantly reduced levels during differentiation. To further investigate downstream consequences, we performed bulk RNA-sequencing at DIV21 and DIV28 (Figure 7A and S7B). In S305N_C1 neurons compared to isogenic WT controls, over 1,200 genes were differentially expressed. Downregulated genes at both DIV21 and DIV28 were significantly enriched for pathways involved in vesicle transport, axon guidance, and synaptic signalling (Figure 7B and S7C). Upregulated genes were enriched in categories related to system development, transcription factor activity, and RNA polymerase II-mediated transcriptional regulation (Figure 7C and S7D). These pathways are consistent with our earlier observations of tubulin blebbing and reduced VGLUT1 expression, indicative of impaired axonal structure and synaptic integrity.

Given the known role of tau in microtubule dynamics, we assessed post-translational modifications (PTMs) of tubulin using immunocytochemistry and immunoblotting. Tyrosinated α-tubulin (Tyr-Tubulin), a marker of dynamic and newly polymerized microtubules[46,47], was more prominently localized in the somatodendritic compartment of S305N-mutant neurons (Figure 7D). Quantitative analysis revealed a significant increase in Tyr-Tubulin signal within MAP2-positive regions of S305N_C1 neurons at both DIV21 and DIV28, with isoHom neurons showing elevated levels only at DIV28 (Figure 7E, F). Longitudinal quantification of Tyr-Tubulin levels showed a progressive decline in WT and isoWT neurons, consistent with the transition toward stable axonal architecture during maturation. In contrast, S305N lines with a homozygous mutation exhibited elevated Tyr-Tub levels compared to their respective WT controls, suggesting altered microtubule dynamics or delayed axonal stabilization (Figure 7G–I). We also investigated tubulin polyglutamylation (PolyE), a PTM that enhances microtubule rigidity and resistance to depolymerization[48]. In WT and isoWT neurons, PolyE-Tubulin levels increased over time, consistent with the formation of stable microtubules. However, S305N_C1 neurons start presenting a decrease in PolyE-Tubulin from DIV14; this change was only significant at DIV28. On the other hand, the isoHet and isoHom S305N neurons had significantly lower levels of polyE-Tubulin from DIV24, and a change was only statistically significant in the isoHet line (Figure 7G, S7E, F). This phenotype is likely driven by the reduced total tau expression and/or the

relative reduction of 3R tau and may underlie the structural and functional axonal impairments observed in this tauopathy model.

A novel neuronal model that can identify modulators of 4R tau.

A major limitation in the field is the lack of high-throughput screening assays to monitor the levels of endogenous 4R tau in human iPSC-derived neurons. To address this, we employed CRISPR/Cas9-mediated genome editing to insert the HiBiT tag at the C-terminus of the MAPT gene in S305N_C1 iPSCs. HiBiT is an 11–amino acid peptide that allows sensitive luminescence-based detection of tagged proteins when complemented with LgBiT in a lytic luminescence assay. Successful integration and expression of HiBiT-tagged tau was confirmed by immunocytochemistry in methanol-fixed neurons using Tau13 and TauC antibodies, both of which colocalised with the HiBiT signal at DIV21 (Figure 8A). To optimise the assay, we treated neurons with a panel of compounds known to affect tau dynamics, including the autophagy inhibitor bafilomycin A1 (Baf), the mTOR inhibitor KU-0063794 (KU), and the small molecule Anle138b, reported to inhibit tau aggregation[49]. After 3 hours of treatment, Baf led to a 50% increase in HiBiT signal, while KU induced a slight reduction. These effects were more pronounced after 20 hours, with Baf significantly increasing tau levels by almost 2-fold and both KU and Anle138b showing a more than 30% reduction (Figure 8B) compared to DMSO-treated cells. Based on this, we selected the 20-hour timepoint for subsequent screening.

Characterisation of S305N_C1 i^3N neurons had revealed that total tau relocated from axonal to somatodendritic compartments (Fig 2B), a redistribution that is known to increase the propensity of tau for aggregation due to reduced microtubule binding. Compounds that can prevent this or modulate the levels of tau overall may be therapeutically relevant. We therefore designed a dual readout platform combining the HiBiT luminescence assay with high-content imaging for phenotypic screening. This setup allows parallel assessment of compound effects on tau levels (via the lytic HiBiT assay), tau localisation (via TauC immunostaining) and cell viability (Figure 8C). To validate the platform, we treated S305N_C1 neurons with Baf or KU for 20 hours. TauC staining confirmed increased tau accumulation with Baf, including a potential increase in axonal tau, while KU treatment resulted in reduced tau staining, consistent with enhanced clearance (Figure 8D). Dose-response experiments with KU and Baf showed concentration-dependent modulation of the HiBiT signal (Figure 8E and F), demonstrating the assay's sensitivity and dynamic range. Notably, neither compound adversely affected cell viability under these conditions; in fact, high concentrations of KU slightly increased viability (~25%), suggesting a potential protective effect. Collectively, these results demonstrate that the HiBiT-tagged S305N_C1 neuronal model provides a robust platform for quantifying changes in 4R tau levels and screening tau-modulating compounds in a high-throughput manner.

Discussion

The human neuron cell lines we describe here represent a significant advancement for the tauopathy field, as they more accurately recapitulate the early disease pathogenesis observed in humans. Prior lines, even those with splice-shifting mutations, only partially model human 4R tauopathies, lacking adequate 4R expression levels or the formation of endogenous seed-competent tau assemblies. It is worth noting that most current neuronal models require multiple tau mutations to increase 4R tau expression, which may limit their physiological relevance[20,21]. The isoHet S305N line is particularly noteworthy as it recapitulates the 1:1 ratio of 3R:4R tau seen in normal adult human brain. Our data demonstrate that the homozygous S305N mutation in MAPT leads to a more than 75% increase in 4R tau, which is associated with alterations in tau expression, phosphorylation, aggregation, and downstream cellular pathways critical for neuronal homeostasis and microtubule stability (see Summary Table S1). These findings expand our understanding of how the disease-associated FTLD-

MAPTS305N mutation can perturb tau homeostasis and contribute to neurodegenerative processes. Clinically, S305N-linked FTLD-MAPT is associated with early-onset disease and rapid progression, and neuropathological studies have identified a predominance of 4R tau pathology, ring-shaped perinuclear tau aggregates, and neurofibrillary tangles[31,39,50]. Our neuronal lines recapitulate much of this phenotype and represent an early stage of this pathogenic process.

We show that S305N_C1 and C2 neurons harbouring the S305N and the IVS10+3 mutations express very high levels of 4R tau throughout differentiation. This isoform imbalance at such an early stage in maturation is particularly noteworthy as proper neuronal development is thought to depend on regulating the expression of both 3R and 4R tau isoforms[51,52]. High levels of 4R tau early on may disrupt key developmental processes, particularly axonogenesis and microtubule organization. Whether this predominance in 4R splicing occurs in humans expressing the S305N mutation during development is not known but it might represent an unusual pathway to tauopathy among the tauopathy-causing mutations. The observation of a marked reduction in total tau protein levels compared to isogenic controls is also significant, as it could exacerbate the destabilization of microtubules and impair axonal transport. The isoHom S305N, based mainly on the immunoblotting analysis, presents a similar phenotype to S305N_C1 neurons in this respect (reduced N-terminus total tau and changes in tubulin PTMs), but at later timepoints (after DIV21). As this is when the levels of 4R MAPT start to increase by more than 70%, the shift towards excessive 4R tau is implicated in altered protein turnover and destabilisation of the axons. Previous studies have shown that 4R tau isoforms have a quicker turnover rate in iPSC-derived neurons[53], which may result in lower tau levels. This may be reflected in the model described here.

The levels of phosphorylated tau were significantly altered in the mutant neuronal lines, particularly in S305N neurons with the homozygous mutation. This was demonstrated by increased CP13 and/or AT8 immunoreactivity, despite overall reduced total tau levels. This suggests a disproportionate phosphorylation of tau, possibly reflecting an early pathological shift. Interestingly, a significant correlation was observed between 4R MAPT mRNA expression and CP13 levels at DIV28, with lower 4R expression associated with an intermediate phenotype and higher expression correlating with a more severe phenotype This dosage effect reinforces the pathogenic role of the S305N mutation and suggests that even partial loss of tau isoform balance can significantly affect neuronal health. We also observed differences in the distribution of the different phosphorylated tau epitopes, with AT100 only being detected in the axons and not in the somatodendritic compartment. The AT100 (pThr212/pSer214) phosphorylation sites are critical for modulating the ability of tau to bind and maintain microtubule stability [54-58]. Phosphorylation of tau at Thr212/Ser214 is thought to play a role in the formation of pathological tau inclusions that accompany the disruption of the structural integrity of neurons[54,58]. Tau hyperphosphorylation at the AT100 epitope may promote or indicate tau detachment from microtubules, increasing its propensity to form small soluble oligomers or insoluble aggregates, which could be toxic to neurons[54-58]. AT100 was increased at DIV28 in all neuronal lines harbouring the S305N mutation, independent of the amount of total tau, and at a timepoint when pFTAA positive signal was present and neurons had formed endogenous, seed-competent tau. The presence of increased AT100 immunoreactive tau in axonal compartments might indicate that tau oligomer formation is initiated there, and that tau seeds are then transported to the soma, where we see the highest accumulation of TOC1 immunoreactive tau and pFTAA. The reasonable timeframe and progressive nature of the tau pathology observed in these neuronal cell lines will make them a valuable tool for assessing the sequence of pathological events during the initial stages and early progression of 4R tauopathies. The appearance of TOC1-positive oligomeric tau, particularly in the perinuclear region and in MAP2-positive compartments, indicates the presence of aggregation-prone tau species. It is worth noting that

similar structures are present in neurons in the cortex of human S305N brain tissue. Importantly, these changes were detected as early as DIV21, and their accumulation increased over time, as confirmed by both immunostaining and live imaging with pFTAA. Notably, we observed pFTAA-positive structures colocalizing with lysosomes, suggesting that pFTAA-positive tau assemblies resist degradation. The absence of tau labelling by MC1, a conformation-specific antibody recognising pathological tau, suggests that despite the accumulation of oligomeric tau, the formation of mature tangle-like pathology may require longer culture times or additional stressors present in the human brain.

The presence of tau seeds in DIV28 neuronal lysates, as shown by the biosensor assay, suggests that S305N neurons not only accumulate misfolded tau, but also generate seed-competent species capable of propagating pathology. The absence of seeding at DIV21, despite detectable TOC1 signal, implies a temporal progression from early oligomeric intermediates to seed-competent assemblies. It is worth also pointing out that generally the seeding signal is on the lower range, possibly due to quite low levels of tau in the neurons, which might make it difficult to identify small changes at DIV21. Our observations support a model where tau misfolding and phosphorylation precede the formation of seed-competent tau species. It is worth noting that isoHet S305N neurons present a trend towards higher TOC1, pFTAA, and seed-competency compared to isoHom S305N. Due to the high density of the i^3N cultures, identifying pFTAA-positive puncta in axons is challenging. However, we did observe some puncta, most of which were located near nuclei or in the pre-axonal segments. Most of the pFTAA signal at DIV28 in fixed cells was observed in MAP2-positive areas and co-localised with TauC which indicates that it selectively identifies tau species in S305N mutant neurons.

Transcriptomic analysis revealed broad changes in gene expression, particularly in pathways related to axon guidance, vesicle trafficking, and synaptic function—key processes that are tightly coupled to microtubule dynamics and tau function. These transcriptomic alterations align with our morphological and biochemical data, including the presence of tubulin blebbing, reduced MAP2 levels, and reduced VGLUT1 expression, which highlight the functional consequences of tau dysregulation. Post-translational modifications of tubulin provide additional insight into the cellular impact. Elevated tyrosinated tubulin and reduced polyglutamylation in the neurons with more than 75% 4R tau suggest a shift toward a more dynamic, less stable microtubule network. These changes are consistent with a failure to mature structurally stable axons. In human AD brain tissue, reductions in acetylated[59] and polyglutamylated[48] α-tubulin have been reported, suggesting that tauopathy affects microtubule structure both *in vitro* and *in vivo*[60].

One of the key current limitations for drug discovery targeting tauopathies is the absence of a high-throughput assay to quantify 4R tau dynamics and functional outcomes in living, human neurons. To address this, we developed a novel luminescence-based assay by knocking in a HiBiT tag at the endogenous *MAPT* C-terminus in the S305N_C1 iPSC line. This system enables rapid, sensitive detection of endogenous tau levels, and offers the added benefit of compatibility with drug screening pipelines. Using the lytic assay, we validated the effects of known tau-modulating compounds. Bafilomycin A1 treatment increased HiBiT signal, reflecting tau accumulation, whereas KU-0063794 and Anle138b reduced tau levels in a time- and concentration-dependent manner. This system also allows phenotypic readouts through high-content imaging, enabling the identification of compounds that not only alter overall tau (C-terminus) levels, but also compounds that affect the subcellular localisation of different tau proteoforms, a key pathological feature in tauopathies and in our cell model. Notably, these lines are the first to report endogenous tau aggregate formation, an important target of therapeutics, which can be monitored longitudinally in these lines. Based on our results, expansion of the toolbelt of S305N mutant lines (including the development of a KOLF background line), or the

refinement of the currently available S305N mutant human neuronal lines (for example, the addition of tags to the NCRAD lines) is now justified.

In conclusion, our study provides an insight into how the accumulation of 4R human tau caused by the S305N mutation disrupts the normal biological function of tau, leading to pathological changes including altered tau, increased phosphorylation and aggregation, impaired microtubule stability, and dysregulation of key neuronal pathways. Our findings not only underscore the multifaceted role of tau in neuronal development and maintenance but also highlight potential therapeutic targets for the earliest stages of tau pathogenesis, and they provide proof-of-concept data for an assay platform to screen them.

Limitations of the study

One limitation of our model is that we used the piggyBac system to introduce hNGN2 into the iPSC lines, which typically results in random integration into the genome. No karyotype abnormalities were observed, but there is still the possibility that hNGN2 could have disrupted some genes in these cells. Replicating some of these findings in either directly differentiated neurons or in iPSC lines where hNGN2 has been introduced into a safe-harbour location will further strengthen our understanding of how the S305N mutation affects neuronal differentiation and tau aggregation.

Resource availability

The data generated and/or analysed in this study are available from the authors upon request.

Bulk RNA-seq data generated as part of this study will be available at the Gene Expression Omnibus

Cell line 802:30F S305N_C1 is a new material generated in this study and available upon request.

Acknowledgments

This work is supported mainly by the Rainwater Charitable Foundation as well as by the UK Dementia Research Institute through UK DRI Ltd, principally funded by the Medical Research Council. We would like to thank NCRAD for the patient derived S305N lines (300.12) and Kathryn Bowles for generating these lines and her advice on the use of the cells. We thank Prof. Selina Wray and her lab for their help and advice on setting up the iPSC cultures, the UCL Drug Discovery Institute for access to equipment and resources, the ALBORADA Drug Discovery Institute for their advice with developing the drug screening assay, Drs Cristina D'Abramo/Peter Davies (The Feinstein Institutes for Medical Research, New York) for CP13 and MC1 antibody, Drs Nicholas Kanaan/Lester Binder (Northwestern University) for TOC1 antibody, Dr Brad Boeve and The Mayo Clinic for human S305N tissue, Dr. David Villaroel (Dr. James Sleigh lab) for the tubulin antibodies and advice and Dr Michael Ward (NIA) for the hNGN2 piggyBac plasmids. Data integrity analysis was performed by Dr Malcolm MacLeod (Edinburgh)

Author contributions

K.E.D conceived the project and E.T designed and performed the experiments. S.B, T.B. M.F, N.W, S.C helped perform experiments and E.T M.B, D.G, E.Tu analysed data. R.C provided protocols and plasmids. E.T wrote the manuscript. All authors discussed, reviewed, and edited the manuscript.

Key resources table

Reagent or Resource	Source	Identifier
Antibodies		
chicken anti-MAP2 (1:2000)	Novus	NB300-213
mouse anti-TUJ1/TUBB3 (1:2000)	Biolegend	801202
chicken anti-NeuN (1:500)	Millipore	ABN9
mouse anti-Tau13 (N-terminus tau, 1:1000)	Santa Cruz Biotechnologies	sc-21796
mouse anti-HT7 tau (Mid-range tau, 1:1000)	Invitrogen	MN1000
rabbit anti-TauC (C-terminus tau, 1:5000)	Daco	A0024
mouse anti- AT8 (1:500)	Invitrogen	MN1020
mouse anti-CP13 (1:500)	Dr. Peter Davies	NA
mouse anti-TOC1 (1:1000)	Dr. Nicholas M. Kanaan	NA
mouse anti-AT100 (1:1000)	Invitrogen	NM1060
rabbit anti-Vglut1 (1:500)	Millipore	MAB5502
mouse anti-HiBiT (1:500)	Promega	N7200
rat anti-Tubulin (tyrosinated tubulin) (1:2000)	Sigma	MAB1864
mouse anti-TRA-1-60 (1:2000)	Abcam	Ab16289
mouse anti-SOX2 (1:1000)	Santa Cruz Biotechnologies	sc-365823
mouse anit-TRA-1-81 (1:2000	Abcam	Ab16289
rabbit anti-NANOG (1:2000	Cell Signalling Technologies	4903S
rabbit anti-PolyE tubulin	Dr. David Villaroel	
Chemicals, peptides, and recombinant proteins		
mTeSR Plus kit	Stem Cell Technologies	100-0276
mTeST1 kit	Stem Cell Technologies	85850
Geltrex	Thermo Fisher Scientific	A1413301
Matrigel	Corning	354277
ReLeSR	Stem Cell Technologies	100-0483
Y-27632	Y-27632	1254/10
Lipofectamine Stem	Thermo Fisher Scientific	STEM00008
DMEM/F-12	Thermo Fisher Scientific	11330032
Doxycycline	Sigma	D9891
Poly-L-Ornithine	Sigma	P3655
Laminin	R&D Systems	3446-005-01
Neurobasal	Thermo Fisher Scientific	21103049
B27 supplement	Thermo Fisher Scientific	17504044
brain-derived neurotrophic factor (BDNF)	PeproTech	450-02
neurotrophin-3 (NT-3)	PeproTech	450-03
CultureOne	Thermo Fisher Scientific	A3320201
Paraformaldehyde	Thermo Fisher Scientific	28908
Intercept Blocking Buffer	LICOR	927-60003
Triton X 100	Sigma	93443
pFTAA	Sigma	SCT066
Tubulin Tracker™ Deep Red	Thermo Fisher Scientific	T34077
RIPA	Thermo Fisher Scientific	89900
cOmplete protease inhibitor cocktail	Roche	11697498001
PhosSTOP	Roche	11697498001
TGX Stain-Free gel	Bio-Rad	5678094

Low-fluorescent PVDF-membranes	Bio-Rad	1620264
SuperBlock TBS blocking buffer	Thermo Fisher Scientific	37535
Invitrogen SDS-PAGE gels	Thermo Fisher Scientific	NP0321BOX
Opti-MEM	Thermo Fisher Scientific	31985062
Lipofectamine 2000	Thermo Fisher Scientific	11668019
Critical commercial assays		
hiPSC Genetic Analysis Kit	Stem Cell Technologies	07550
Pierce BCA protein assay kit	Thermo	23227
MultiTox-Fluor Multiplex Cytotoxicity Assay	Promega	G9200
Nano-Glo HiBiT Lytic Detection Reagent	Promega	N3040
Experimental models: Cell lines		
802:30F (WT)	Current study	
802:30F_S305N/IVS10+3_HiBiT (S305N_C1, D4)	Current study	
802:30F_S305N/IVS10+3_HiBiT (S305N_C1, G8)	Current study	
300.12-NWBB7 (isoWT, IUGB249.1-iso5)	NCRAD	https://ncrad.iu.edu Bowles *et al*[28]
300.12-NW1C7 (isoHet S305N, IUGB249.1.2)	NCRAD	https://ncrad.iu.edu Bowles *et al*[28]
300.12-HCB8 (isoHom S305N, IUGB249.1-iso3)		https://ncrad.iu.edu Bowles *et a.l*[28]
Tau RD S305N-YFP HEK293 biosensors	Available from Prof. Karen Duff	Watamura *et al.*[29]
Software and algorithms		
Prism 10.5.0	GraphPad	https://www.graphpad.com/
Harmony 5.1	Revvity	
Photoshop Elements 2020	Adobe	
ImageLab	BioRad	

Methods

Generation of iPSC line with a S305N/IVS10+3 mutation via CRISPR-Cas9

For the generation of iPSC with a double mutation, S305N and IVS10+3 were generated by Synthego utilising one of their in-house iPSC lines (802:30F). Briefly, a single guide (GUACUCACACUGCCGCCUCC) was utilised to introduce both mutations by using their in-house CRISP-Cas9 editing protocol. Sanger sequencing was utilised to identify clones with homozygote double mutation. Consequently, one of the clones (Clone B11) carrying the double homozygote mutation was selected to knock in a HiBit tag in the C-terminus of *MAPT*. Two clones were provided (D4 and G8) from Synthego that contained the double mutant and the HiBiT tag (S305N_C1 and C2) as well as the mock transfected wild-type cells (WT).

Culture of iPSC

iPSC on the 802:30F background were maintained in Geltrex (Thermo; A1413301) coated plates using mTeSR Plus (StemCell Technologies; 100-0276) and passaged using 0.5 mM EDTA (Thermo; 15575-020). Patient-derived iPSC on the 300.12 background were obtained from NCRAD. These cells were maintained in Matrigel (Corning, 354277) using mTeSR1 (StemCell Technologies; 85850) and

passaged using ReLeSR (Stem Cell Technologies; 100-0483). All iPSC lines for this work were regularly tested for mycoplasma.

Stable integration of piggyBac plasmids into iPSCs

To generate stably expressing hNGN2-expressing iPSC we integrated a BFP-containing doxycycline-induced hNGN2 cassette using the piggyBac system. iPSCs were washed with PBS, dissociated with Accutase (Gibco; A1110501), and plated into coated plates (Geltrex or Matrigel) at $1x10^6$ cells/well of a 6-well plate in mTeSR Plus or mTeSR1 containing 10 µM Y-27632 (Tocris; 1254/10). Once cells were attached, they were washed with PBS before being transfected with constructs containing the donor doxycycline-induced hNGN2 and BFP fluorescent reporter flanked by transposon terminal repeats and the piggyBac transposase. For the transfection 3 µg of total plasmid DNA was used (2:1 donor to transposase ratio), with Lipofectamine Stem (Thermo; STEM00008) as per the manufacturer's instructions. Forty-eight hours post-transfection, media was changed and supplemented with 1 µg/mL puromycin for 3 days to select for cells that had successfully integrated the hNGN2. To obtain a pure population of cells with high levels of BFP expression from thorough cassette insertion, cells were subjected to fluorescence-activated cell sorting (FACS) using BFP fluorescence. To ensure genomic stability, iPSCs were karyotyped by using low-coverage sequencing (UCL Genomics) with 1Mb resolution. All lines were also checked routinely for abnormalities by using the hiPSC Genetic Analysis Kit (Stem Cell Technologies, 07550).

iPSC differentiation into cortical i^3N neurons

Induction of iPSC into cortical neurons was initiated by dissociating cells in Accutase and plating $1x10^6$ iPSC onto Geltrex (Synthego 802:30F lines) or Matrigel (NCRAD 300.12 lines) coated 6-well plates using DMEM/F-12 with Glutamax/Hepes (Thermo, 11330032) containing 2 µg/mL doxycycline (Sigma; D9891), 1X N2 Supplement (Thermo, 17502048), 1X non-essential amino acids (Thermo, 11140050) and 10 µM Y-27632. The media was replaced daily for the next 2 days with media without Y-27632. At day 3, induced cells were dissociated with Accutase and replated into plates double-coated with 0.1 mg/mL Poly-L-Ornithine (PLO; Sigma, P3655; 24 hours at 37°C) and 30 µg/mL Laminin (R&D Systems, 3446-005-01; 24-72 hours at 37°C). Cells were plated into 6-well plates at $0.6x10^6$ cells/well, 24-well plates at $0.125x10^6$ cells/well, into 96-well Phenoplates (Revvity; 6055300) or white plates for Luminescence assays (Greiner, 655083) at 30,000 cells/well. Neuronal maturation media consisted of Neurobasal (Thermo, 21103049) media containing 1X B27 (Thermo, 17504044), 10 ng/mL brain-derived neurotrophic factor (BDNF, PeproTech, 450-02), 10 ng/mL neurotrophin-3 (NT-3, PeproTech, 450-03), 6-12 µg/mL Laminin, 2 µg/mLl doxycycline, and 1X CultureOne (Thermo, A3320201). Once a week, one-half of the media was replaced with fresh media until cells were collected.

Immunocytochemistry, imaging, and analysis

Human iPSCs were fixed with 4% methanol-free paraformaldehyde (Thermo; 28908) diluted in PBS for 15 min at room temperature and washed 3 times in DPBS (Thermo; 14190-094). Most of the i^3N neurons were fixed with 100% methanol for 15 min at -20° C. Cells were washed twice with ice-cold DPBS. Cells were blocked/permeabilised with Intercept Blocking Buffer (LICOR; 927-60003) containing 0.1% Triton (Sigma; 93443) for 1 hour at room temperature. Primary antibodies diluted in blocking buffer were added to the cells and incubated overnight at 4°C and then washed twice with DPBS. The following primary antibodies were used: chicken anti-MAP2 (1:2000, Novus; NB300-213), mouse anti-TUJ1/TUBB3 (1:2000, Biolegend; 801202), chicken anti-NeuN (1:500, Millipore; ABN9), mouse anti-Tau13 (N-terminus tau, 1:1000, Santa Cruz Biotechnologies; sc-21796), mouse anti-HT7

tau (Mid-range tau, 1:1000, Invitrogen; MN1000), rabbit anti-TauC (C-terminus tau, 1:5000, Daco; A0024), mouse anti-AT8 (1:500, Invitrogen; MN1020), mouse anti-CP13 (1:500, Peter Davies), mouse anti-TOC1 (1:1000, Nicholas M. Kanaan) mouse anti-AT100 (1:1000, Invitrogen; NM1060), rabbit anti-VGLUT1 (1:500, Millipore; MAB5502), mouse anti-HiBiT (1:500, Promega, N7200), rat anti-Tubulin (tyrosinated α-tubulin) (1:2000, Sigma; MAB1864), mouse anti-TRA-1-60 (1:2000, Abcam; Ab16289), mouse anti-SOX2 (1:1000, Santa Cruz Biotechnologies; sc-365823), mouse anit-TRA-1-81 (1:2000, Abcam; Ab16289) and rabbit anti-NANOG (1:2000, Cell Signalling Technologies; 4903S). Secondary antibodies diluted in blocking buffer, including goat anti-mouse, anti-rabbit or anti-chicken conjugated with Alexa Fluor 488, Alexa Fluor 568 or Alexa Fluor 647 (1:1000) as well as Hoechst (1:1000, Thermo; 33342) were added into the cells and incubated for 1 hour at room temperature. Cells were washed twice with DPBS.

Images were acquired with the high-content microscope Opera Phenix Plus (Revvity) by using the 40x water immersion objective with 12 fields of view per well and z-stack of 6 planes (0.5 µm per plane). Acquisition settings (exposure times and laser power) were adjusted to be above the camera background and kept below saturation levels. Imaging settings were kept the same between biological replicates.

Acquired images were analysed in Harmony 5.1. Briefly, a stack of each image was maximum projected and basic flatfield correction was applied. Cells were segmented by identifying the nuclei of live cells only ('find nuclei building block'). 'Find image region' was used to identify tau or Tubulin in the imaged field. For antibodies where staining was localised in the soma, such as TOC1 or AT8, MAP2 was used to identify cytoplasm and consequently 'find image region with absolute thresholding' was used to identify the TOC1 positive area. In some cases, TOC1 stained dead cells, and a filter was applied to remove these areas during the analysis. Both intensity and area of the studied protein were calculated, and the results were normalised to the number of cells. Integrated intensity was calculated by multiplying the area by the mean intensity. Due to variation in the absolute values of the integrated intensity between biological replicates, Z-scoring was used instead. For each biological experiment, the Z-score was calculated with the formula $Zi = \frac{\mathrm{Xi}-\mu}{\sigma}$, where Xi is the value of the individual technical replicate, μ is the mean of all conditions for the specific biological experiment and σ is the standard deviation for all conditions for the specific biological experiment. Average Z-scores from different biological replicates were plotted in GraphPad Prism.

pFTAA live imaging of i^3N neurons and imaging analysis

To monitor pFTAA staining in i^3N neurons, cells were grown until DIV25. Old media was aspirated, and cells were washed with fresh Neurobasal media without Phenol Red (Thermo; 12348017) containing 1X B27 (Thermo, 17504044), 10 ng/mL brain-derived neurotrophic factor (BDNF, PeproTech, 450-02), 10 ng/mL neurotrophin-3 (NT-3, PeproTech, 450-03), 6-12 µg/mL Laminin, 2 µg/mL doxycycline and 1X CultureOne (Thermo, A3320201) to remove dead cell from the culture. Fresh neuronal media containing 1.5 µM pFTAA (Sigma, SCT066) and 1:10000 Tubulin Tracker™ Deep Red (Thermo, T34077) was added and plates were incubated for 30 min before starting live imaging on the high-content microscope Opera Phenix Plus by using the 63x water immersion objective with 9 fields of view per well and z-stack of 6 planes (0.5 µm) with the environmental control enabled (5% CO_2, 37° C and humidity). Images were acquired every 9 h for four continuous days. The pFTAA signal was detected by using 405nm/550nm Ex/Em filters and Tubulin at 647nm/665nm Ex/Em, BFP was also imaged as a nuclei marker (375nm/450nm Ex/Em, it is part of the hNGN2 plasmid). For experiments where we fixed cells after staining with pFTAA, a similar approach was followed; however, plates were maintained in the incubator before fixation with methanol and staining.

Acquired images were analysed in Harmony 5.1. Briefly, a stack of each image was maximum projected, and basic flatfield correction was applied. Live cells were identified by the 'find nuclei' (using the BFP channel) function, bead cells were filtered out using a different approach such as nuclei size and intensity. The cytoplasm of living cells was then identified using the tubulin channel (cytoplasm was only considered areas that had tubulin staining). 'Find regions building block' was used to identify pFTAA positive areas by using the absolute threshold option to make sure that we detected objects above background (600-700 was used as the lowest threshold). Objects where pFTAA was colocalised with dead cells were excluded from the analysis by filtering them out. Both pFTAA area and intensity were calculated and normalised to the number of live cells. Results are presented as integrated intensity, and data were plotted on GraphPad Prism.

Quantitative PCR (qPCR)

iPSCs samples for RNA extraction were collected by washing cells with PBS and dissociating cells with either EDTA or ReLeSa, spinning down at 300xg for 7 min at 4ºC. Pellets were stored at -80ºC. i^3N neurons were washed with PBS before adding fresh PBS and lifting the monolayer by swirling the plate. Cells were collected and spun down at 300xg for 7 min at 4ºC and pellets were stored at -70ºC. RNA extraction was performed by using ReliaPrep RNA Cell Miniprep System (Promega; Z6012) according to the manufacturer's instructions. Reverse transcription was performed by using 300 ng RNA and LunaScript RT Supermix Kit (New England Biolabs; E3010) by following the manufacturer's instructions. qPCR was performed using the Luna Universal qPCR Master Mix kit (New England Biolabs; M3003S), according to the manufacturer's instructions and reactions were carried out using the Lightcycler 480 II (Roche). Expression values were calculated in Excel by using the Ct method, where GAPDH was used as a control.

Semi-quantitative PCR (sq-PCR)

Semi-quantitative PCR was conducted to quantify the ratio of 3R:4R mRNA. cDNA was used as a template, which amplified by primers[61] flanking exon 10 (forward 5'-AAGTCGCCGTCTTCCGCCAAG-3'; reverse 5' -GTCCAGGGACCCAATCTTCGA-3'). Q5 2x master mix (New England Biolabs; M0492S) was used for the amplification, and PCR products were run on a 2% agarose gel with 381bp and 288bp fragments indicating 4R and 3R, respectively. Ratios were calculated as previously described[62], where ImageJ box plots and measure plots were used. Sum pixel intensity values were exported into Excel, and percentage change was calculated by dividing each isoform value by the summed total intensity.

Sample preparation for bulk RNAseq, sequencing, data processing, and analysis

All iPSC lines were differentiated into neurons on 24-well plates, and samples were collected at DIV21 and DIV28 post-induction. Samples were washed with PBS and the neuronal monolayer was collected on fresh PBS and spun down at 300xg for 7 min at 4ºC, and pellets were stored at -80ºC until RNA extraction was performed with ReliaPrep RNA Cell Miniprep System (Promega; Z6012). Extracted RNA was sent to Novogene (Cambridge, UK) where quality control was performed by using the Agilent 5400 to determine sample quantitation, integrity, and purity. mRNA was purified from total RNA using poly-T oligo-attached magnetic beads. After fragmentation, the first strand cDNA was synthesized using random hexamer primers, followed by the second strand cDNA synthesis using dTTP for non-directional library, which was ready after end repair, A-tailing, adapter ligation, size selection, amplification, and purification. Samples were sequenced in NovaSeq 6000 (Illumina) with pair-end 100 cycles. Raw data (raw reads) of FASTQ format were first processed through in-house Perl scripts. In this step, clean data (clean reads) were obtained by removing reads containing adapter, reads containing

ploy-N and low-quality reads from raw data. At the same time, Q20, Q30 and GC content of the clean data were calculated. All the downstream analyses were based on clean data with high quality. Reference genome and gene model annotation files were downloaded from the genome website directly. Index of the reference genome was built using Hisat2 v2.0.5. Reads were aligned to the reference human genome (GRCH38) using Hisat2 v2.0.5. featureCounts v1.5.0-p3 was used to count the reads mapped to each gene. And then FPKM of each gene was calculated based on the length of the gene and the reads count mapped to this gene. FPKM, expected number of Fragments Per Kilobase of transcript sequence per Millions base pairs sequenced, considers the effect of sequencing depth and gene length for the read count at the same time. Differential expression analysis of two groups (2-3 biological replicates per condition) was performed using the DESeq2 R package. The resulting P-values were adjusted using Benjamini and Hochberg's approach for controlling the false discovery rate. Genes with an adjusted P-value <=0.05 found by DESeq2 were assigned as differentially expressed. To find enriched annotations with the hot genes, gene ontology was performed using gProfiler (https://biit.cs.ut.ee/gprofiler/gost), where annotations of canonical pathways, biological processes, cellular compartments and molecular function were determined for the hit genes.

Immunoblot analysis

All iPSC lines were differentiated into neurons on 6-well plates and samples were collected at DIV7, 10, 14, 17, 21, 24, 28 post-induction. Briefly, cells were washed with DPBS once before adding RIPA (Thermo; 89900) buffer containing cOmplete protease inhibitor cocktail (Roche; 11697498001) and PhosSTOP (Roche; 11697498001). Lysates were incubated on ice for 30 min, centrifuged at 12,000 g for 10 min at 4ºC, and supernatants were collected. Samples for dephosphorylation assay were lysed in 50 mM Tris pH 7.6, 0.15 M NaCl, cOmplete protease inhibitor cocktail. Protein concentration was determined by using Pierce BCA protein assay kit (Thermo; 23227) for all lysates. Equal amount was loaded into 4-20% TGX Stain-Free gel (Bio-Rad; 5678094) or dephosphorylated with lambda-phosphatase (Santa Cruz Biotechnology; sc-200312A). Low-fluorescent PVDF-membranes (Bio-Rad; 1620264) was used to transfer the proteins and blocked with 5% milk in TBS-Tween (0.02% Tween). Primary antibodies were diluted in SuperBlock TBS blocking buffer (Thermo Fisher Scientific; 37535) and incubated overnight at 4ºC. The next primary antibodies were used: mouse anti-Tau13 (N-terminus tau, 1:1000, Santa Cruz Biotechnologies; sc-21796), mouse anti-HT7 tau (Mid-range tau, 1:1000, Invitrogen; MN1000), rabbit anti-TauC (C-terminus tau, 1:5000, Daco, A0024), mouse anti- AT8 (1:500, Invitrogen, MN1020), mouse anti-CP13 (1:500, Peter Davies), rat anti-Tubulin (tyrosinated tubulin) (1:2000, Sigma; MAB1864), rabbit anti-PolyE tubulin (1:5000, gift from David Villaroel), anti-β- actin-FITC (Millipore, F3022). Incubation with AT8 antibody was not compatible with the TGX Stain-Free gel for that reason, 4-12% SDS-PAGE gels (Invitrogen, NP0321BOX) were used. Secondary HRP-conjugated goat anti-rabbit or goat anti-mouse antibodies were diluted in 5% milk in TBS-Tween for 1 hour at room temperature. Chemiluminescence (BioRad) was used for detection of immunoblotting and bands were quantified by intensity using ImageLab (BioRad). For the current study all, blotted membranes were stripped by using PLUS Western Blot Stripping Buffer (Thermo Fisher, 10016433) for 12 min before incubating with a new primary antibody.

Sample preparation for seeding with i^3N neurons

i^3N neurons were plates into 6-well plates and samples for seeding were collected at DIV21 and DIV28. A whole 6-well plate was used for these experiments. Cells were washed with DPBS before adding fresh DPBS and lifting cells as a monolayer by swirling the plate. Cells were pelleted by centrifuging at 300g for 7 min at 4ºC and stored at -80ºC. Pellets were lysed with 50 mM Tris pH 7.6, 0.15 M NaCl, cOmplete protease inhibitor cocktail. Samples were sonicated with a water bath sonicator (Qsonica

Q800R3) at 4°C for 5 min at 65 amplitude (30 seconds on, 60 seconds off) before incubating on ice for 30 min. Samples were spun down at 300g for 5 min at 4ºC and supernatant was collected. Protein concentration was determined by using Pierce BCA protein assay kit.

Biosensor cell culture method, seeding, and imaging

Tau RD S305N-YFP HEK293 biosensors were cultured in DMEM (Thermo Fisher, cat. no. 41966-029) with 10% FBS and 1% Pen-Strep. Cells were plated at a density of 33,000 cells/well in a 96-well plate PhenoPlates (Revvity), in a volume of 130 µl medium per well. After 18 hours, cells were transduced with seeds; 1.25 µl Lipofectamine 2000 (Thermo Fisher Scientific, 11668019) was mixed with 8.75 µl Opti-MEM (Thermo Fisher Scientific, 31985062) and incubated at room temperature for 5 min before mixing with 18 µg of total protein of i^3N neurons total lysates. Complexes were incubated for 30 min at 37ºC before transferring 20 µl in each well and were incubated for 72 hours. For each condition, three technical replicates were included.

Before imaging 1:10000 Hoechst was added to the cells and incubated for 10 min. Plate was imaged on the high-content microscope Opera Phenix Plus by using the 20x water immersion objective with 20 fields of view per well and a z-stack of 8 planes (0.8 µm) with the environmental control enabled (5% CO_2, 37ºC, and humidity). Excitation wavelengths and emission filters were used as follows: YFP 488 nm, 527-530 nm, Hoechst: 375 nm, 435–480 nm. The acquired images were analysed in Harmony 5.2. Briefly, images were loaded as maximum projection and basic flatfield correction was applied. Cells were segmented by using the "find nuclei" building block using the Hoechst channel, consequently, "find cytoplasm" was identified by using the watershed of the Hoechst channel. The YFP positive tau inclusions were identified by using the "find spots" building block (method C) on the YFP channel. The analysis was exported, and the number of spots per nuclei was calculated.

HiBiT Lytic detection assay and Viability assay

For the lytic assay, neurons were grown in white, Cellstar plates until DIV20 at 100 µl maintenance media. Neurons were treated at the indicated timepoint. To assess the neuronal viability at the final timepoint the GF-AFC substrate from MultiTox-Fluor Multiplex Cytotoxicity Assay (Promega, G9200) was used following the manufacturer's protocol. Briefly, 20 µl from the 5x GF-AFC substrate was added into the cells, incubated for 30 min at 37 °C before reading fluorescence (400Ex/505Em) at the FLUOstar Omega plate reader (BMG Labtech). Afterwards, 120 µl of the Nano-Glo HiBiT Lytic Detection Reagent (Promega, N3040) was added directly to the cells and incubated for 10 min before recording luminescence on a FLUOstar Omega plate reader with 0.2 s integration time.

Human tissue

Human brain sample was kindly provided from Mayo Clinic.

Immunohistochemistry

For human FFPE staining, 8 µm sections were deparaffinized in xylene and rehydrated using graded alcohols. Following pressure cooker pretreatment in citrate buffer for 10 min and endogenous peroxidase quenching for 10 min, sections were blocked in 10% dried milk solution. Tissue sections were incubated with primary antibodies tau antibodies for 1 hour at room temperature, followed by biotinylated secondary incubation for 30 min at room temperature and avidin-biotin complex for 30 min. Colour was developed with 3,3′-diaminobenzidine/H_2O_2. Sections were scanned on a NanoZoomer Digital Pathology C9600 (Hamamatsu Photonics).

Statistical analysis

All statistical analysis was conducted at GraphPad Prism. T-test was used to compare two groups and One-way ANOVA for three groups or more, with the appropriate post-hoc test as stated in the figure legend. Two-way ANOVA was used for comparison between cell lines and time with the appropriate post-hoc test.

Reference

1. Götz, J., Halliday, G., and Nisbet, R.M. (2019). Molecular Pathogenesis of the Tauopathies. Annual Review of Pathology: Mechanisms of Disease *14*, 239-261. https://doi.org/10.1146/annurev-pathmechdis-012418-012936.
2. Brunello, C.A., Merezhko, M., Uronen, R.L., and Huttunen, H.J. (2020). Mechanisms of secretion and spreading of pathological tau protein. Cell Mol Life Sci *77*, 1721-1744. 10.1007/s00018-019-03349-1.
3. Feinstein, S.C., and Wilson, L. (2005). Inability of tau to properly regulate neuronal microtubule dynamics: a loss-of-function mechanism by which tau might mediate neuronal cell death. Biochimica et Biophysica Acta (BBA) - Molecular Basis of Disease *1739*, 268-279. https://doi.org/10.1016/j.bbadis.2004.07.002.
4. Goedert, M., Spillantini, M.G., Jakes, R., Rutherford, D., and Crowther, R.A. (1989). Multiple isoforms of human microtubule-associated protein tau: sequences and localization in neurofibrillary tangles of Alzheimer's disease. Neuron *3*, 519-526. https://doi.org/10.1016/0896-6273(89)90210-9.
5. Goedert, M., and Jakes, R. (1990). Expression of separate isoforms of human tau protein: correlation with the tau pattern in brain and effects on tubulin polymerization. The EMBO Journal *9*, 4225-4230-4230. https://doi.org/10.1002/j.1460-2075.1990.tb07870.x.
6. Hefti, M.M., Farrell, K., Kim, S., Bowles, K.R., Fowkes, M.E., Raj, T., and Crary, J.F. (2018). High-resolution temporal and regional mapping of MAPT expression and splicing in human brain development. PLoS One *13*, e0195771. 10.1371/journal.pone.0195771.
7. Trabzuni, D., Wray, S., Vandrovcova, J., Ramasamy, A., Walker, R., Smith, C., Luk, C., Gibbs, J.R., Dillman, A., Hernandez, D.G., et al. (2012). MAPT expression and splicing is differentially regulated by brain region: relation to genotype and implication for tauopathies. Hum Mol Genet *21*, 4094-4103. 10.1093/hmg/dds238.
8. Beevers, J.E., Lai, M.C., Collins, E., Booth, H.D.E., Zambon, F., Parkkinen, L., Vowles, J., Cowley, S.A., Wade-Martins, R., and Caffrey, T.M. (2017). MAPT Genetic Variation and Neuronal Maturity Alter Isoform Expression Affecting Axonal Transport in iPSC-Derived Dopamine Neurons. Stem Cell Reports *9*, 587-599. 10.1016/j.stemcr.2017.06.005.
9. Conrad, C., Zhu, J., Conrad, C., Schoenfeld, D., Fang, Z., Ingelsson, M., Stamm, S., Church, G., and Hyman, B.T. (2007). Single molecule profiling of tau gene expression in Alzheimer's disease. Journal of Neurochemistry *103*, 1228-1236. https://doi.org/10.1111/j.1471-4159.2007.04857.x.
10. Rösler, T.W., Tayaranian Marvian, A., Brendel, M., Nykänen, N.P., Höllerhage, M., Schwarz, S.C., Hopfner, F., Koeglsperger, T., Respondek, G., Schweyer, K., et al. (2019). Four-repeat tauopathies. Prog Neurobiol *180*, 101644. 10.1016/j.pneurobio.2019.101644.
11. Stamelou, M., Respondek, G., Giagkou, N., Whitwell, J.L., Kovacs, G.G., and Höglinger, G.U. (2021). Evolving concepts in progressive supranuclear palsy and other 4-repeat tauopathies. Nature Reviews Neurology *17*, 601-620. 10.1038/s41582-021-00541-5.
12. Karch, C.M., Kao, A.W., Karydas, A., Onanuga, K., Martinez, R., Argouarch, A., Wang, C., Huang, C., Sohn, P.D., Bowles, K.R., et al. (2019). A Comprehensive Resource for Induced Pluripotent Stem Cells from Patients with Primary Tauopathies. Stem Cell Reports *13*, 939-955. https://doi.org/10.1016/j.stemcr.2019.09.006.
13. Mahali, S., and Karch, C. (2021). Defective proteostasis in patient-derived iPSC-astrocytes and neurons carrying a MAPT IVS10+16 mutation. Alzheimer's & Dementia *17*, e058727. https://doi.org/10.1002/alz.058727.
14. Silva, M.C., Cheng, C., Mair, W., Almeida, S., Fong, H., Biswas, M.H.U., Zhang, Z., Huang, Y., Temple, S., Coppola, G., et al. (2016). Human iPSC-Derived Neuronal Model of Tau-A152T Frontotemporal Dementia Reveals Tau-Mediated Mechanisms of Neuronal Vulnerability. Stem Cell Reports *7*, 325-340. 10.1016/j.stemcr.2016.08.001.
15. Wray, S. (2017). Modeling tau pathology in human stem cell derived neurons. Brain Pathol *27*, 525-529. 10.1111/bpa.12521.
16. Handel, A.E., Chintawar, S., Lalic, T., Whiteley, E., Vowles, J., Giustacchini, A., Argoud, K., Sopp, P., Nakanishi, M., Bowden, R., et al. (2016). Assessing similarity to primary tissue and

cortical layer identity in induced pluripotent stem cell-derived cortical neurons through single-cell transcriptomics. Hum Mol Genet *25*, 989-1000. 10.1093/hmg/ddv637.

17. Sposito, T., Preza, E., Mahoney, C.J., Setó-Salvia, N., Ryan, N.S., Morris, H.R., Arber, C., Devine, M.J., Houlden, H., Warner, T.T., et al. (2015). Developmental regulation of tau splicing is disrupted in stem cell-derived neurons from frontotemporal dementia patients with the 10 + 16 splice-site mutation in MAPT. Hum Mol Genet *24*, 5260-5269. 10.1093/hmg/ddv246.
18. Verheyen, A., Diels, A., Reumers, J., Van Hoorde, K., Van den Wyngaert, I., van Outryve d'Ydewalle, C., De Bondt, A., Kuijlaars, J., De Muynck, L., De Hoogt, R., et al. (2018). Genetically Engineered iPSC-Derived FTDP-17 MAPT Neurons Display Mutation-Specific Neurodegenerative and Neurodevelopmental Phenotypes. Stem Cell Reports *11*, 363-379. 10.1016/j.stemcr.2018.06.022.
19. Miguel, L., Rovelet-Lecrux, A., Feyeux, M., Frebourg, T., Nassoy, P., Campion, D., and Lecourtois, M. (2019). Detection of all adult Tau isoforms in a 3D culture model of iPSC-derived neurons. Stem Cell Res *40*, 101541. 10.1016/j.scr.2019.101541.
20. García-León, J.A., Cabrera-Socorro, A., Eggermont, K., Swijsen, A., Terryn, J., Fazal, R., Nami, F., Ordovás, L., Quiles, A., Lluis, F., et al. (2018). Generation of a human induced pluripotent stem cell–based model for tauopathies combining three microtubule-associated protein TAU mutations which displays several phenotypes linked to neurodegeneration. Alzheimer's & Dementia *14*, 1261-1280. https://doi.org/10.1016/j.jalz.2018.05.007.
21. Parra Bravo, C., Giani, A.M., Madero-Perez, J., Zhao, Z., Wan, Y., Samelson, A.J., Wong, M.Y., Evangelisti, A., Cordes, E., Fan, L., et al. (2024). Human iPSC 4R tauopathy model uncovers modifiers of tau propagation. Cell *187*, 2446-2464.e2422. https://doi.org/10.1016/j.cell.2024.03.015.
22. Capano, L.S., Sato, C., Ficulle, E., Yu, A., Horie, K., Kwon, J.S., Burbach, K.F., Barthélemy, N.R., Fox, S.G., Karch, C.M., et al. (2022). Recapitulation of endogenous 4R tau expression and formation of insoluble tau in directly reprogrammed human neurons. Cell Stem Cell *29*, 918-932.e918. 10.1016/j.stem.2022.04.018.
23. Hutton, M., Lendon, C.L., Rizzu, P., Baker, M., Froelich, S., Houlden, H., Pickering-Brown, S., Chakraverty, S., Isaacs, A., Grover, A., et al. (1998). Association of missense and 5'-splice-site mutations in tau with the inherited dementia FTDP-17. Nature *393*, 702-705. 10.1038/31508.
24. Hasegawa, M., Smith, M.J., Iijima, M., Tabira, T., and Goedert, M. (1999). FTDP-17 mutations N279K and S305N in tau produce increased splicing of exon 10. FEBS Lett *443*, 93-96. 10.1016/s0014-5793(98)01696-2.
25. Spillantini, M.G., and Goedert, M. (2013). Tau pathology and neurodegeneration. Lancet Neurol *12*, 609-622. 10.1016/s1474-4422(13)70090-5.
26. Boeve, B.F., Tremont-Lukats, I.W., Waclawik, A.J., Murrell, J.R., Hermann, B., Jack, C.R., Jr., Shiung, M.M., Smith, G.E., Nair, A.R., Lindor, N., et al. (2005). Longitudinal characterization of two siblings with frontotemporal dementia and parkinsonism linked to chromosome 17 associated with the S305N tau mutation. Brain *128*, 752-772. 10.1093/brain/awh356.
27. Kobayashi, K., Kidani, T., Ujike, H., Hayashi, M., Ishihara, T., Miyazu, K., Kuroda, S., and Koshino, Y. (2003). Another phenotype of frontotemporal dementia and parkinsonism linked to chromosome-17 (FTDP-17) with a missense mutation of S305N closely resembling Pick's disease. J Neurol *250*, 990-992. 10.1007/s00415-003-1137-6.
28. Bowles, K.R., Pedicone, C., Pugh, D.A., Oja, L.-M., Sousa, F.H., Keavey, L.K., Fulton-Howard, B., Weitzman, S.A., Liu, Y., Chen, J.L., et al. (2024). Development of MAPT S305 mutation human iPSC lines exhibiting elevated 4R tau expression and functional alterations in neurons and astrocytes. Cell Reports *43*, 115013. https://doi.org/10.1016/j.celrep.2024.115013.
29. Watamura, N., Foiani, M.S., Bez, S., Bourdenx, M., Santambrogio, A., Frodsham, C., Camporesi, E., Brinkmalm, G., Zetterberg, H., Patel, S., et al. (2025). In vivo hyperphosphorylation of tau is associated with synaptic loss and behavioral abnormalities in the absence of tau seeds. Nat Neurosci *28*, 293-307. 10.1038/s41593-024-01829-7.
30. Chen, J.L., Moss, W.N., Spencer, A., Zhang, P., Childs-Disney, J.L., and Disney, M.D. (2019). The RNA encoding the microtubule-associated protein tau has extensive structure that affects its biology. PLoS One *14*, e0219210. 10.1371/journal.pone.0219210.

31. Iijima, M., Tabira, T., Poorkaj, P., Schellenberg, G.D., Trojanowski, J.Q., Lee, V.M., Schmidt, M.L., Takahashi, K., Nabika, T., Matsumoto, T., et al. (1999). A distinct familial presenile dementia with a novel missense mutation in the tau gene. Neuroreport *10*, 497-501. 10.1097/00001756-199902250-00010.
32. Spillantini, M.G., Murrell, J.R., Goedert, M., Farlow, M.R., Klug, A., and Ghetti, B. (1998). Mutation in the tau gene in familial multiple system tauopathy with presenile dementia. Proc Natl Acad Sci U S A *95*, 7737-7741. 10.1073/pnas.95.13.7737.
33. Pantazis, C.B., Yang, A., Lara, E., McDonough, J.A., Blauwendraat, C., Peng, L., Oguro, H., Kanaujiya, J., Zou, J., Sebesta, D., et al. (2022). A reference human induced pluripotent stem cell line for large-scale collaborative studies. Cell Stem Cell *29*, 1685-1702.e1622. https://doi.org/10.1016/j.stem.2022.11.004.
34. Fernandopulle, M.S., Prestil, R., Grunseich, C., Wang, C., Gan, L., and Ward, M.E. (2018). Transcription Factor-Mediated Differentiation of Human iPSCs into Neurons. Curr Protoc Cell Biol *79*, e51. 10.1002/cpcb.51.
35. Seo, W.M., Yoon, J., Lee, J.-H., Lee, Y., Lee, H., Geum, D., Sun, W., and Song, M.-R. (2022). Modeling axonal regeneration by changing cytoskeletal dynamics in stem cell-derived motor nerve organoids. Scientific Reports *12*, 2082. 10.1038/s41598-022-05645-6.
36. Faris, H., Almasieh, M., and Levin, L.A. (2021). Axonal degeneration induces distinct patterns of phosphatidylserine and phosphatidylethanolamine externalization. Cell Death Discovery *7*, 247. 10.1038/s41420-021-00641-7.
37. Chu, D., Yang, X., Wang, J., Zhou, Y., Gu, J.H., Miao, J., Wu, F., and Liu, F. (2024). Tau truncation in the pathogenesis of Alzheimer's disease: a narrative review. Neural Regen Res *19*, 1221-1232. 10.4103/1673-5374.385853.
38. Quinn, J.P., Corbett, N.J., Kellett, K.A.B., and Hooper, N.M. (2018). Tau Proteolysis in the Pathogenesis of Tauopathies: Neurotoxic Fragments and Novel Biomarkers. J Alzheimers Dis *63*, 13-33. 10.3233/jad-170959.
39. Kobayashi, K., Hayashi, M., Kidani, T., Ujike, H., Iijima, M., Ishihara, T., Nakano, H., Sugimori, K., Shimazaki, M., Kuroda, S., and Koshino, Y. (2004). Pick's disease pathology of a missense mutation of S305N of frontotemporal dementia and parkinsonism linked to chromosome 17: another phenotype of S305N. Dement Geriatr Cogn Disord *17*, 293-297. 10.1159/000077157.
40. Whitwell, J.L., Jack, C.R., Jr., Boeve, B.F., Senjem, M.L., Baker, M., Ivnik, R.J., Knopman, D.S., Wszolek, Z.K., Petersen, R.C., Rademakers, R., and Josephs, K.A. (2009). Atrophy patterns in IVS10+16, IVS10+3, N279K, S305N, P301L, and V337M MAPT mutations. Neurology *73*, 1058-1065. 10.1212/WNL.0b013e3181b9c8b9.
41. Ward, S.M., Himmelstein, D.S., Lancia, J.K., Fu, Y., Patterson, K.R., and Binder, L.I. (2013). TOC1: characterization of a selective oligomeric tau antibody. J Alzheimers Dis *37*, 593-602. 10.3233/jad-131235.
42. Holmes, B.B., Furman, J.L., Mahan, T.E., Yamasaki, T.R., Mirbaha, H., Eades, W.C., Belaygorod, L., Cairns, N.J., Holtzman, D.M., and Diamond, M.I. (2014). Proteopathic tau seeding predicts tauopathy in vivo. Proc Natl Acad Sci U S A *111*, E4376-4385. 10.1073/pnas.1411649111.
43. Neumann, M., Mittelbronn, M., Simon, P., Vanmassenhove, B., de Silva, R., Lees, A., Klapp, J., Meyermann, R., and Kretzschmar, H.A. (2005). A new family with frontotemporal dementia with intronic 10+3 splice site mutation in the tau gene: neuropathology and molecular effects. Neuropathol Appl Neurobiol *31*, 362-373. 10.1111/j.1365-2990.2005.00629.x.
44. Brelstaff, J., Ossola, B., Neher, J.J., Klingstedt, T., Nilsson, K.P.R., Goedert, M., Spillantini, M.G., and Tolkovsky, A.M. (2015). The fluorescent pentameric oligothiophene pFTAA identifies filamentous tau in live neurons cultured from adult P301S tau mice. Frontiers in Neuroscience *Volume 9 - 2015*. 10.3389/fnins.2015.00184.
45. Brelstaff, J., Spillantini, M.G., and Tolkovsky, A.M. (2015). pFTAA: a high affinity oligothiophene probe that detects filamentous tau: in vivo: and in cultured neurons. Neural Regeneration Research *10*, 1746-1747. 10.4103/1673-5374.165298.

46. Fu, G., Yan, S., Khoo, C.J., Chao, V.C., Liu, Z., Mukhi, M., Hervas, R., Li, X.D., and Ti, S.-C. (2023). Integrated regulation of tubulin tyrosination and microtubule stability by human α-tubulin isotypes. Cell Reports *42*, 112653. https://doi.org/10.1016/j.celrep.2023.112653.
47. Sanyal, C., Pietsch, N., Ramirez Rios, S., Peris, L., Carrier, L., and Moutin, M.-J. (2023). The detyrosination/re-tyrosination cycle of tubulin and its role and dysfunction in neurons and cardiomyocytes. Seminars in Cell & Developmental Biology *137*, 46-62. https://doi.org/10.1016/j.semcdb.2021.12.006.
48. Genova, M., Grycova, L., Puttrich, V., Magiera, M.M., Lansky, Z., Janke, C., and Braun, M. (2023). Tubulin polyglutamylation differentially regulates microtubule-interacting proteins. Embo j *42*, e112101. 10.15252/embj.2022112101.
49. Hosseini-Gerami, L., Ficulle, E., Humphryes-Kirilov, N., Airey, D.C., Scherschel, J., Kananathan, S., Eastwood, B.J., Bose, S., Collier, D.A., Laing, E., et al. (2023). Mechanism of action deconvolution of the small-molecule pathological tau aggregation inhibitor Anle138b. Alzheimers Res Ther *15*, 52. 10.1186/s13195-023-01182-0.
50. Skoglund, L., Viitanen, M., Kalimo, H., Lannfelt, L., Jönhagen, M.E., Ingelsson, M., Glaser, A., and Herva, R. (2008). The tau S305S mutation causes frontotemporal dementia with parkinsonism. Eur J Neurol *15*, 156-161. 10.1111/j.1468-1331.2007.02017.x.
51. Lacovich, V., Espindola, S.L., Alloatti, M., Pozo Devoto, V., Cromberg, L.E., Čarná, M.E., Forte, G., Gallo, J.M., Bruno, L., Stokin, G.B., et al. (2017). Tau Isoforms Imbalance Impairs the Axonal Transport of the Amyloid Precursor Protein in Human Neurons. J Neurosci *37*, 58-69. 10.1523/jneurosci.2305-16.2016.
52. McMillan, P., Korvatska, E., Poorkaj, P., Evstafjeva, Z., Robinson, L., Greenup, L., Leverenz, J., Schellenberg, G.D., and D'Souza, I. (2008). Tau isoform regulation is region- and cell-specific in mouse brain. J Comp Neurol *511*, 788-803. 10.1002/cne.21867.
53. Sato, C., Barthélemy, N.R., Mawuenyega, K.G., Patterson, B.W., Gordon, B.A., Jockel-Balsarotti, J., Sullivan, M., Crisp, M.J., Kasten, T., Kirmess, K.M., et al. (2018). Tau Kinetics in Neurons and the Human Central Nervous System. Neuron *97*, 1284-1298.e1287. 10.1016/j.neuron.2018.02.015.
54. Regalado-Reyes, M., Furcila, D., Hernández, F., Ávila, J., DeFelipe, J., and León-Espinosa, G. (2019). Phospho-Tau Changes in the Human CA1 During Alzheimer's Disease Progression. J Alzheimers Dis *69*, 277-288. 10.3233/jad-181263.
55. Ksiezak-Reding, H., He, D., Gordon-Krajcer, W., Kress, Y., Lee, S., and Dickson, D.W. (2000). Induction of Alzheimer-specific tau epitope AT100 in apoptotic human fetal astrocytes. Cell Motility *47*, 236-252. https://doi.org/10.1002/1097-0169(200011)47:3<236::AID-CM6>3.0.CO;2-K.
56. Alonso, A.D., Cohen, L.S., Corbo, C., Morozova, V., ElIdrissi, A., Phillips, G., and Kleiman, F.E. (2018). Hyperphosphorylation of Tau Associates With Changes in Its Function Beyond Microtubule Stability. Front Cell Neurosci *12*, 338. 10.3389/fncel.2018.00338.
57. Alonso, A.D., Di Clerico, J., Li, B., Corbo, C.P., Alaniz, M.E., Grundke-Iqbal, I., and Iqbal, K. (2010). Phosphorylation of tau at Thr212, Thr231, and Ser262 combined causes neurodegeneration. J Biol Chem *285*, 30851-30860. 10.1074/jbc.M110.110957.
58. Yoshida, H., and Goedert, M. (2006). Sequential phosphorylation of tau protein by cAMP-dependent protein kinase and SAPK4/p38delta or JNK2 in the presence of heparin generates the AT100 epitope. J Neurochem *99*, 154-164. 10.1111/j.1471-4159.2006.04052.x.
59. Hempen, B., and Brion, J.P. (1996). Reduction of acetylated alpha-tubulin immunoreactivity in neurofibrillary tangle-bearing neurons in Alzheimer's disease. J Neuropathol Exp Neurol *55*, 964-972. 10.1097/00005072-199609000-00003.
60. Cook, C., Carlomagno, Y., Gendron, T.F., Dunmore, J., Scheffel, K., Stetler, C., Davis, M., Dickson, D., Jarpe, M., DeTure, M., and Petrucelli, L. (2013). Acetylation of the KXGS motifs in tau is a critical determinant in modulation of tau aggregation and clearance. Human Molecular Genetics *23*, 104-116. 10.1093/hmg/ddt402.
61. Choi, S.H., Kim, Y.H., Hebisch, M., Sliwinski, C., Lee, S., D'Avanzo, C., Chen, H., Hooli, B., Asselin, C., Muffat, J., et al. (2014). A three-dimensional human neural cell culture model of Alzheimer's disease. Nature *515*, 274-278. 10.1038/nature13800.

62. Antiabong, J.F., Ngoepe, M.G., and Abechi, A.S. (2016). Semi-quantitative digital analysis of polymerase chain reaction-electrophoresis gel: Potential applications in low-income veterinary laboratories. Vet World *9*, 935-939. 10.14202/vetworld.2016.935-939.

Figure legends

Figure 1: i^3N neurons with the S305N mutation express predominantly 4R MAPT.

(A) Schematic representation of the used iPSC lines and generation of iPSC lines with the piggyBachNGN2 system, which allows neuronal differentiation (created with Biorender). (B) Representative semi-qPCR of 3R and 4R MAPT levels overtime. Quantification of (C) 4R MAPT and (D) 3R MAPT from B (n=4-7 separate neuronal differentiations). (E) Total mRNA levels of MAPT qualified by qPCR (n=4-7 independent neuronal differentiations). (F) Representative images of methanol-fixed i^3N neurons from DIV21 and DIV28 stained with TUJ1, MAP2, and NeuN. (G) Total mRNA levels of MAP2 as measured by qPCR (n=3-5). Quantification of MAP2 expression levels from (F) in the 802:30F lines and (I) 300.12 lines (Two-way ANOVA with Tukey post-test, ****, $p<0.0001$, n=3-4 independent neuronal differentiations).

Figure 2: Distribution of total tau in i^3N neurons with S305N mutations.

(A) Map of full-length tau and epitope sites of the used total tau antibodies (created by Biorender). (B) Representative images of DIV21 and DIV28 i^3N neurons double-stained with MAP2 and one of the total tau antibodies: Tau13 (left side), HT7 (middle), and TauC (right). Quantification of (C-D) Tau13, (E-F) HT7 and (G-H) TauC in all neuronal lines compared to their isogenic WT controls. Two-way ANOVA with Tukey post-test, n=3-5 independent neuronal differentiations for (C-H).

Figure 3: Distribution of phosphorylated tau on i^3N neurons with S305N mutations.

(A) Map of full-length tau and epitope sites of the total phosphorylated tau antibodies used (created by Biorender). (B) Representative images of DIV21 and DIV28 i^3N neurons double-stained with MAP2 and one of the phosphorylated tau antibodies: AT8 (left side), CP13 (middle), and AT100 (right). Quantification of total (C-D) AT8, (E-F) CP13, and (G-H) AT100 in all neuronal lines compared to isogenic WT controls. Two-way ANOVA with Tukey post-test, n=3-4 independent neuronal differentiations for (C-H).

Figure 4: Temporal analysis of total and phosphorylated tau on i^3N neurons with S305N mutations.

(A) Representative immunoblots for different total tau (Tau13: top, HT7: middle, and TauC: bottom) and pTau (CP13, AT8 bottom) in all neuronal lines overtime. Stain-free or actin was used as a loading control, as indicated. Red arrows indicate early phosphorylation. Quantification of expression levels of total tau antibodies (B) Tau13/Total protein (C) TauC/Total protein at DIV10, 21, and 28 for all lines. Quantification of expression levels of pTau antibodies (D) CP13/TauC and (E) AT8/TauC at DIV10, 21 and 28 for all neuronal lines. Statistical analysis was conducted between the mutated lines and their respective isogenic WT controls. Unpaired t-test for S305N_C1 vs WT and Freidman One-way ANOVA for isoHet/isoHom S305N vs isoWT. The above tests were selected due to the difficulty in comparing immunoblots between experimental replicates. *, $p<0.05$; **, $p<0.01$; ***, $p<0.001$. n=2-3 independent neuronal differentiations.

Figure 5: i^3N neurons with a S305N mutation form endogenous seed-competent tau.

(A) Representative images of TOC1 co-stained with MAP2 (top panel and zoomed in) or TUJ1 (bottom panel and zoomed in) in DIV28 from all neuronal lines. (B) Quantification of TOC1 from DIV28 i^3N neurons (t-test for S305N_C1 vs WT and One-way ANOVA followed by Tukey post-hoc test for isoHet and isoHom S305N vs isoWT, for n=4-5 independent neuronal differentiations). (C) Representative images of tau seeding activity in S305N biosensors seeded with DIV28 i^3N neurons lysates from all

lines. (D) Quantification of the seeding activity at DIV28 in the S305N biosensors (One-way ANOVA followed by Tukey post-hoc. n=3 independent neuronal differentiations). (E) Representative images of human tissue from patients with either S305N mutation stained for AT8, CP13, TOC1 and MC1. (F) Quantification of seeding activity from the human frozen S305N brain tissue.

Figure 6: pFTAA positive inclusion on i^3N neurons with S305N mutations.

(A) Representative images of i^3N neurons stained live with pFTAA and Tubulin overtime. Dyes were added at DIV25, and images were acquired every 9 hours. (B) Quantification of pFTAA signal in Tubulin positive area overtime in WT and S305N_C1 neurons (two-way ANOVA, Tukey post-hoc test, n=3 independent neuronal differentiations). (C) Quantification of pFTAA signal in Tubulin positive area overtime in isoWT and isoHet and isoHom S305N neurons (two-way ANOVA, Tukey post-hoc test, n=3 independent neuronal differentiation). (D) Representative images of pFTAA co-stained with TauC in DIV28 neurons fixed with methanol. (E) Representative images showing colocalization of pFTAA with TOC1 and MAP2 in DIV28 neurons fixed with methanol. *, $p<0.05$; **, $p<0.01$; ***, $p<0.001$; ****, $p<0.0001$.

Figure 7: i^3N neurons with a S305N mutation present cytoskeleton change.

(A) Volcano plot comparing differently expressed genes between S305N_C1 and WT i^3N neurons at DIV28. Gene set enrichment analysis pathways identified from downregulated (B) and upregulated (C) DEGs in S305N_C1 vs. WT neurons at DIV28. Significantly enriched GO terms for biological process, cellular component, and molecular function. (D) Representative staining of Tyr-Tubulin on i^3N neurons from DIV21 and DIV28 for all neuronal lines. (E) Quantification of Tyr-Tubulin in MAP2 area in WT vs S305N_C1 neurons at DIV21 and DIV28 (Two-way ANOVA, Tukey post-hoc test, n= 2 independent neuronal differentiations). (F) Quantification of Tyr-Tubulin in MAP2 area in isoWT vs isoHet and isoHom S305N neurons at DIV21 and DIV28 (Two-way ANOVA, Tukey post-hoc test, n=2-3 independent neuronal differentiation). (G) Representative immunoblots of Tyr-Tubulin overtime (top panel) and PolyE-Tubulin (bottom panel) in all neuronal lines. Quantification of protein levels of Tyr-Tubulin in WT vs S305N_C1 neurons (H) and isoWT vs isoHet/isoHom S305N (two-way ANOVA Tukey post-hoc test, n=2-3 independent neuronal differentiations). *, $p<0.05$; **, $p<0.01$.

Figure 8: Optimisation of a drug screen assay for 4R tau modulators.

(A) Representative images showing co-localisation of HiBiT tag with Tau13 (left) or TauC (right) at DIV21 neurons. (B) Changes in luminescence levels after treatment with DMSO, 10 nM Baf, 10 µM Ku or 10 nM Anle138b for 3 or 20 hours at DIV21 (Two-way ANOVA Tukey post-hoc test, n=2 independent neuronal differentiations). (C) Schematic representations of a proposed screening platform for 4R tau modifiers (created with Biorender). (B) Representative images of methanol-fixed neurons stained with TauC and MAP2 after treatment with DMSO, 10 nM Baf and 10 µM Ku for 20 hours (DIV21 neurons). Dose response changes in luminescence/HiBiT and Viability of DIV21 S305N_C1 neurons treated with (E) Ku or (F) Baf for 20 hours. *, $p<0.05$; **, $p<0.01$; ***, $p<0.001$; ****, $p<0.0001$.

Figure S1: Characterisation of iPSC with S305N tau mutation

(A) Schematic representation of the inserted mutations in the 802:30F line to generate the S305N_C1 and C2 iPSC lines. (B) mRNA expression levels of the pluripotent markers (B) NANOG and (C) SOX2 in all lines at DIV0 (iPSC) and DIV28 (i^3N neurons). (C) Low-coverage sequencing showed no abnormalities in the WT, S305N_C1 and C2 iPSC lines after insertion of hNGN2. (D) Pluripotency

marker staining TRA-1-60/SOX2 and TRA-1-81/NANOG confirms iPSC pluripotency in all iPSC lines after the insertion of hNGN2.

Figure S2: Characterising i^{3}N neurons with S305N tau mutation related to figure 1

Expression levels of TUJ1 in the WT and S305N_C1 and C2 (A) and isoWT, isoHet, and isoHom S305N (B) lines at DIV21 and 28 (Two-way ANOVA, n=3 independent neuronal differentiations). (C) NeuN-positive neurons in all lines at DIV21 and 28 (Two-way ANOVA, n=3). (D) VGLU1 mRNA levels in all lines overtime (n=3-5). (E) Representative images of VGLUT1 staining in all neuronal lines at DIV21 and 28. Cells were fixed with 4% PFA. Quantification of VGLUT1 WT and S305N_C1 and C2 (F) and isoWT, isoHet, and isoHom S305N (G) lines at DIV21 and DIV28 (Two-way ANOVA Tukey post-hoc test, n=3). **, $p<0.01$; ****, $p<0.0001$

Figure S3: Distribution of total and phosphorylated tau on i^{3}N neurons with a S305N mutation related to figures 2 and 3

(A) Representative images of TauC with TUJ1 co-staining for all neuronal lines. (B) Representative images of CP13 and TauC co-staining for all neuronal lines. (C) Expression levels of AT8 immunostaining normalised to TauC in the WT and S305N_C1 neurons at DIV21 and DIV28 (Two-way ANOVA, Tukey post-hoc test, n=3 independent neuronal differentiations). (D) Expression levels of CP13 immunostaining normalised to TauC in the WT and S305N_C1 neurons at DIV21 and 28 (Two-way ANOVA, Tukey post-hoc test, n=3).

Figure S4: Overtime expression levels of total and phosphorylated tau related to figure 4

Overtime protein levels of total tau (A) Tau13 (B) TauC, and (C) HT7 antibodies normalised to total protein (stain free) in all neuronal lines. Overtime expression of CP13 (phosphorylated tau) normalised (D) to total protein and (E) TauC in all neuronal lines. Overtime protein levels of AT8 (phosphorylated tau) normalised (F) to total protein and (G) TauC in all neuronal lines. Protein levels of HT7 (left), CP13 (middle) and AT8 (right) at (H) DIV10, (I) DIV21 and (J) DIV28 normalised to total protein (stain free) in all neuronal lines. (K) Protein levels of CP13 (Left) and AT8 (right) normalised to TauC at DIV7 in the isoWT, isoHet and isoHom S305N. (L) Representative immunoblots of dephosphorylation assay for tau in all neuronal lines at DIV21 and DIV28. Tau13 was used to detect the different isoforms. Unpaired t-test for S305N_C1 vs WT and Freidman One-way ANOVA for isoHet and isoHom S305N vs isoWT. The above tests were selected due to the difficulty in comparing immunoblots between independent neuronal differentiations. *, $p<0.05$; **, $p<0.01$. n=2-3 independent neuronal differentiations.

Figure S5: TOC1 expression at DIV21 and colocalization with Tau13 S305N i^{3}N neurons related to Figure 5.

(A) Representative images of TOC1 and MAP2 co-staining at DIV21 for all neuronal lines. (B) Representative images of TOC1 and TUJ1 co-staining at DIV21 for all neuronal lines. (C) Representative images of TOC1 and Tau13 co-staining at DIV28 for all neuronal lines. (D) Quantification of TOC1 from DIV21 i^{3}N neurons (t-test for S305N_C1 vs WT and One-way ANOVA followed by Tukey post-hoc test for isoHet and isoHom S305N vs isoWT, for n=4-5 independent neuronal differentiations). (I) Quantification of the seeding activity at DIV21 in the S305N biosensors (One-way ANOVA followed by Tukey post-hoc, n=3 independent neuronal differentiations).

Figure S6: pFTAA colocalizes with LysotrackerRed in S305N_C1 i^{3}N neurons and bulk RNAseq analysis from DIV21 S305N_C1 i^{3}N neurons related to figures 6 and 7.

(A) Representative images of WT and S305N_C1 neurons stained with pFTAA, LysotrackerRed and Tubulin (TUBB) at DIV28. (B) Volcano plot comparing differently expressed genes between S305N_C1 and WT i^3N neurons at DIV21. Gene set enrichment analysis pathways identified from downregulated (C) and upregulated (D) DEGs in S305N-C1 vs. WT neurons at DIV21. Significantly enriched GO terms for biological process, cellular component, and molecular function. (E) Quantification of PolyE Tubulin normalised to total protein over time in all neuronal lines. (two-way ANOVA Tukey post-hoc test, n=2 independent neuronal differentiations). *, $p<0.05$.

Table S1: Summary of changes in 4R MAPT, total tau, phosphorylated tau and hyperphosphorylated tau (pTau/TauC) in all lines with S305N mutation. Data were either normalised to cell number for the ICC or loading control for the WB. [1] Protein levels of phosphorylated tau were normalised to loading control, [2] Protein levels of phosphorylated tau were normalised to TauC levels.

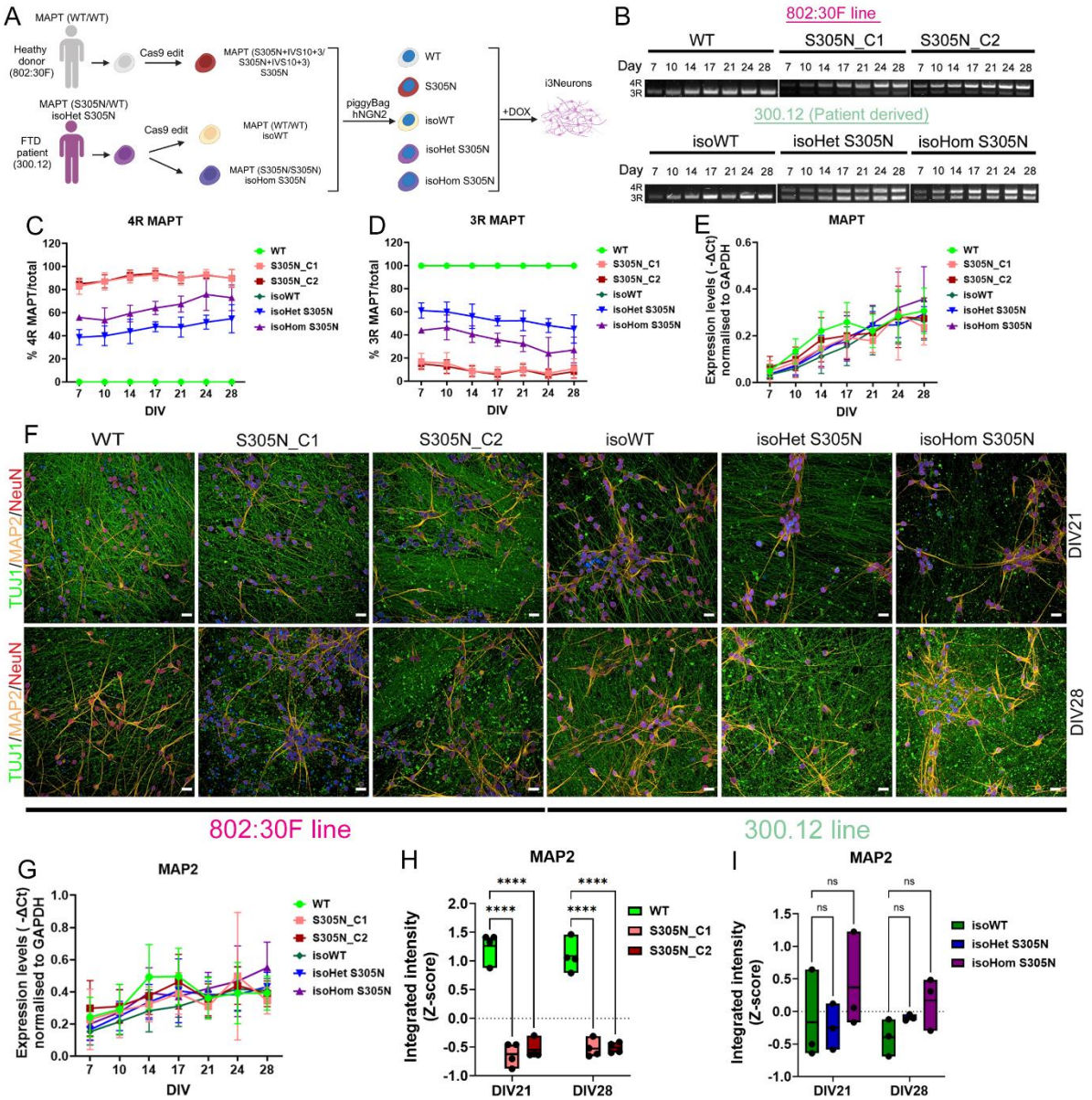
A
MAPT (WT/WT)
Heathy donor (802:30F)
Cas9 edit
MAPT (S305N+IVS10+3/ S305N+IVS10+3) S305N
MAPT (S305N/WT) isoHet S305N
FTD patient (300.12)
Cas9 edit
MAPT (WT/WT) isoWT
MAPT (S305N/S305N) isoHom S305N
piggyBag hNGN2
WT
S305N
isoWT
isoHet S305N
isoHom S305N
+DOX
i3Neurons
B
802:30F line
WT
S305N_C1
S305N_C2
Day 7 10 14 17 21 24 28
4R
3R
300.12 (Patient derived)
isoWT
isoHet S305N
isoHom S305N
C
4R MAPT
% 4R MAPT/total
DIV
D
3R MAPT
% 3R MAPT/total
E
MAPT
Expression levels (-ΔCt) normalised to GAPDH
F
TUJ1/MAP2/NeuN
DIV21
DIV28
802:30F line
300.12 line
G
MAP2
H
Integrated intensity (Z-score)
****
I
ns

Figure 1

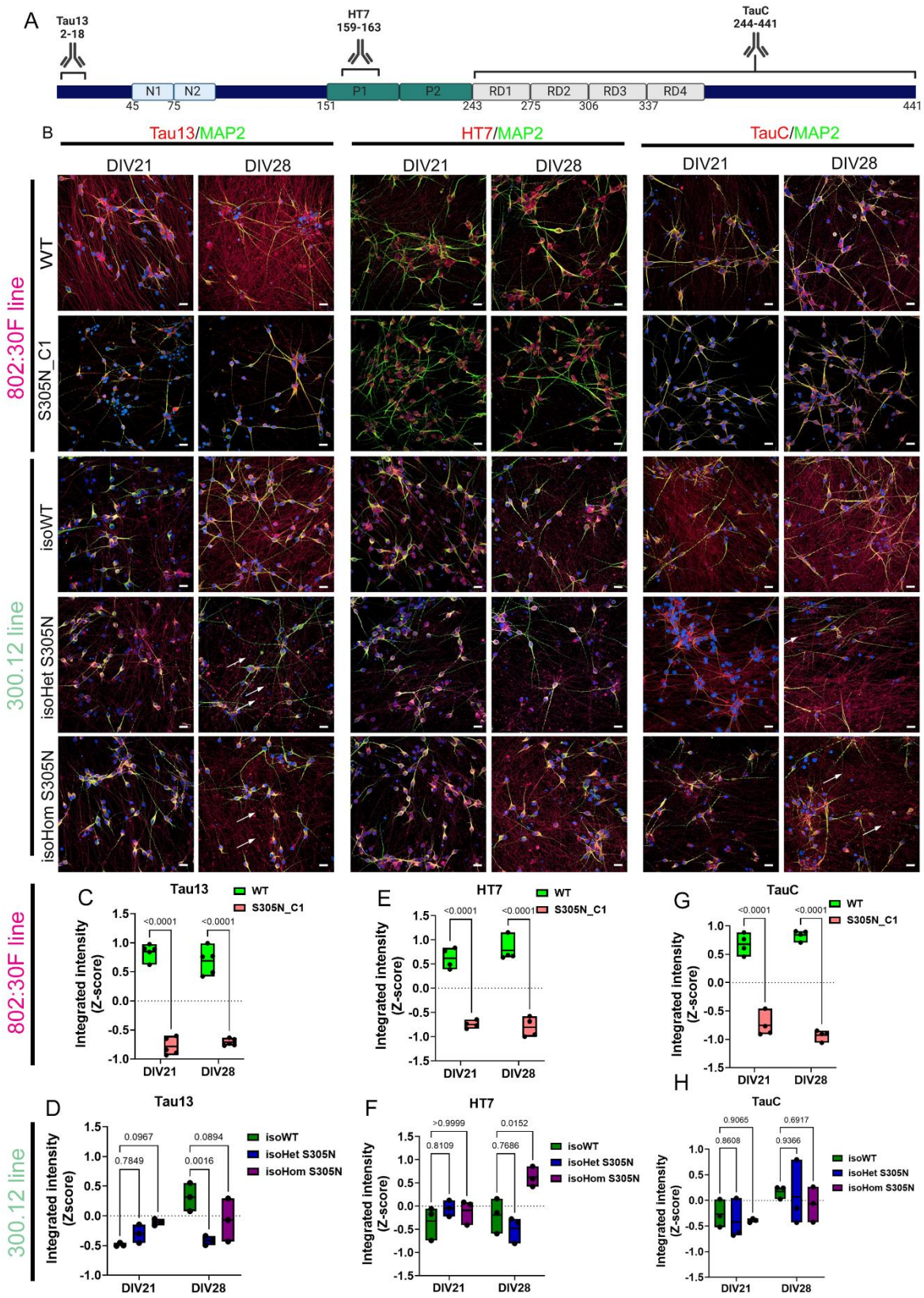
A
Tau13
2-18
HT7
159-163
TauC
244-441
N1
N2
P1
P2
RD1
RD2
RD3
RD4
45
75
151
243
275
306
337
441
B
Tau13/MAP2
HT7/MAP2
TauC/MAP2
DIV21
DIV28
802:30F line
WT
S305N_C1
300.12 line
isoWT
isoHet S305N
isoHom S305N
C
Tau13
WT
S305N_C1
Integrated intensity (Z-score)
<0.0001
DIV21
DIV28
E
HT7
G
TauC
H
D
Tau13
Integrated intensity (Zscore)
0.0967
0.7849
0.0894
0.0016
isoWT
isoHet S305N
isoHom S305N
F
HT7
>0.9999
0.8109
0.0152
0.7686
TauC
0.9065
0.8608
0.6917
0.9366

Figure 2

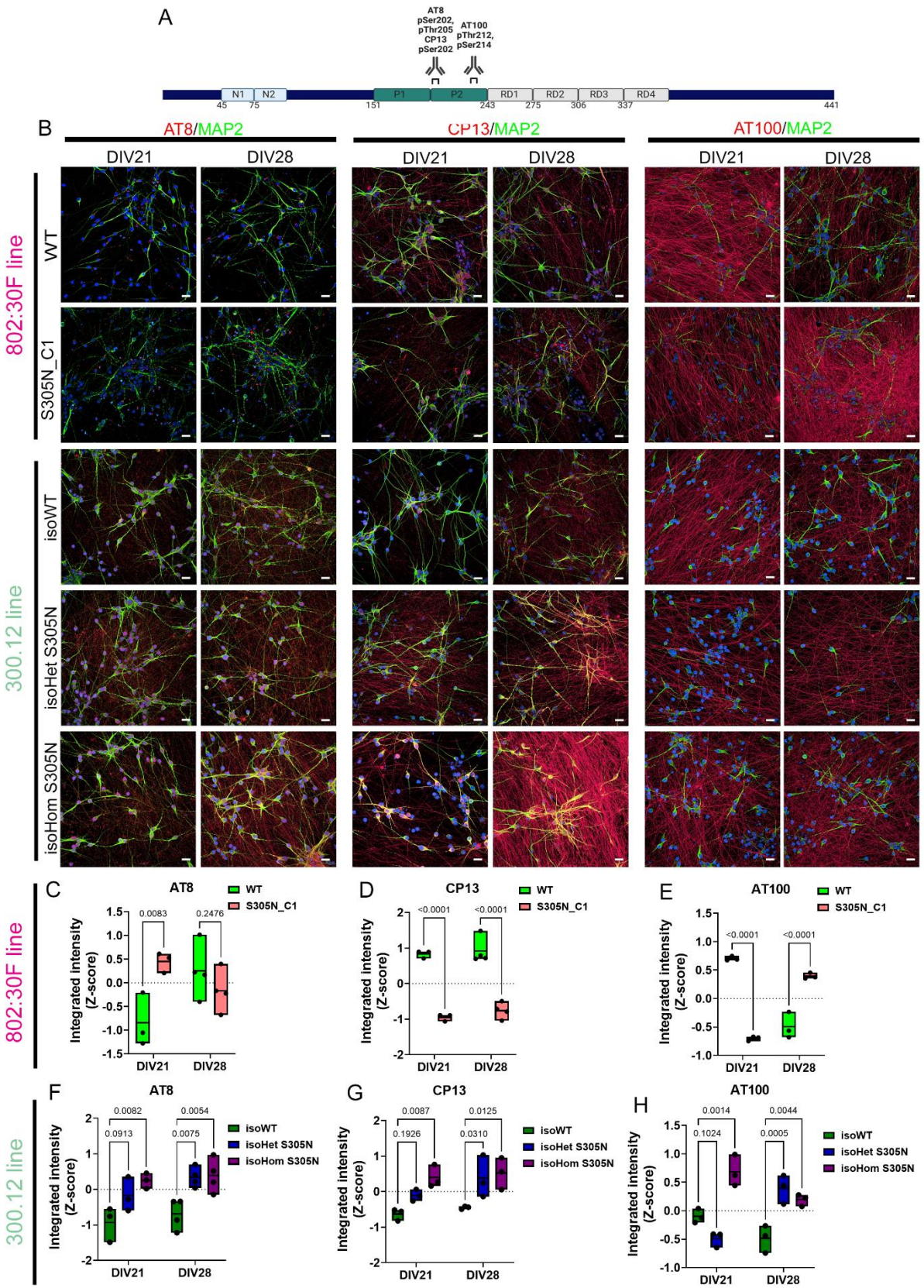
A
AT8
pSer202,
pThr205
CP13
pSer202
AT100
pThr212,
pSer214
N1
N2
P1
P2
RD1
RD2
RD3
RD4
45
75
151
243
275
306
337
441
B
AT8/MAP2
CP13/MAP2
AT100/MAP2
DIV21
DIV28
802:30F line
WT
S305N_C1
300.12 line
isoWT
isoHet S305N
isoHom S305N
C
AT8
WT
S305N_C1
0.0083
0.2476
Integrated intensity (Z-score)
DIV21
DIV28
D
CP13
<0.0001
<0.0001
E
AT100
<0.0001
<0.0001
F
AT8
isoWT
isoHet S305N
isoHom S305N
0.0082
0.0913
0.0054
0.0075
G
CP13
0.0087
0.1926
0.0125
0.0310
H
AT100
0.0014
0.1024
0.0044
0.0005

Figure 3

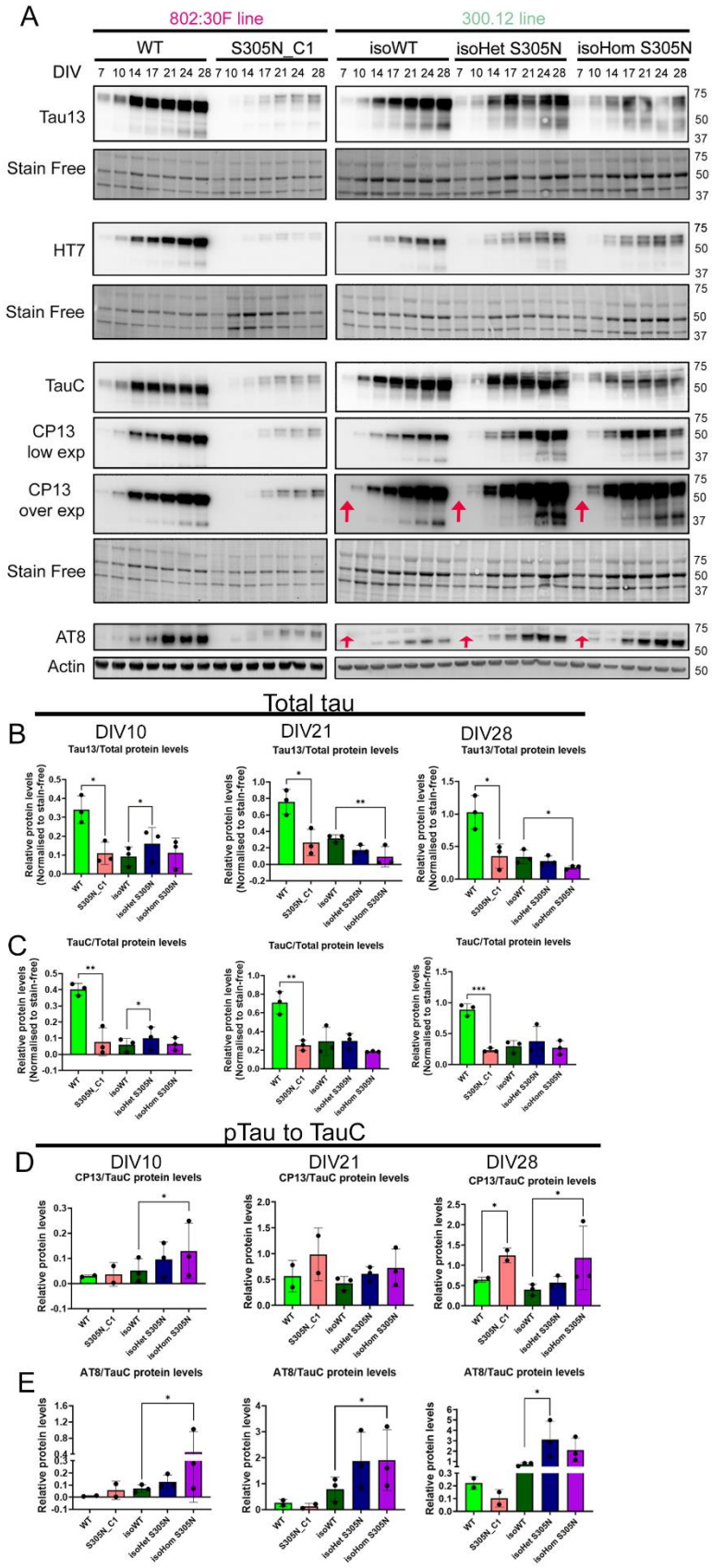
A
802:30F line
300.12 line
WT
S305N_C1
isoWT
isoHet S305N
isoHom S305N
DIV
7 10 14 17 21 24 28
Tau13
Stain Free
HT7
TauC
CP13 low exp
CP13 over exp
AT8
Actin
75
50
37
Total tau
B
DIV10
DIV21
DIV28
Tau13/Total protein levels
Relative protein levels (Normalised to stain-free)
C
TauC/Total protein levels
pTau to TauC
D
CP13/TauC protein levels
Relative protein levels
E
AT8/TauC protein levels

Figure 4

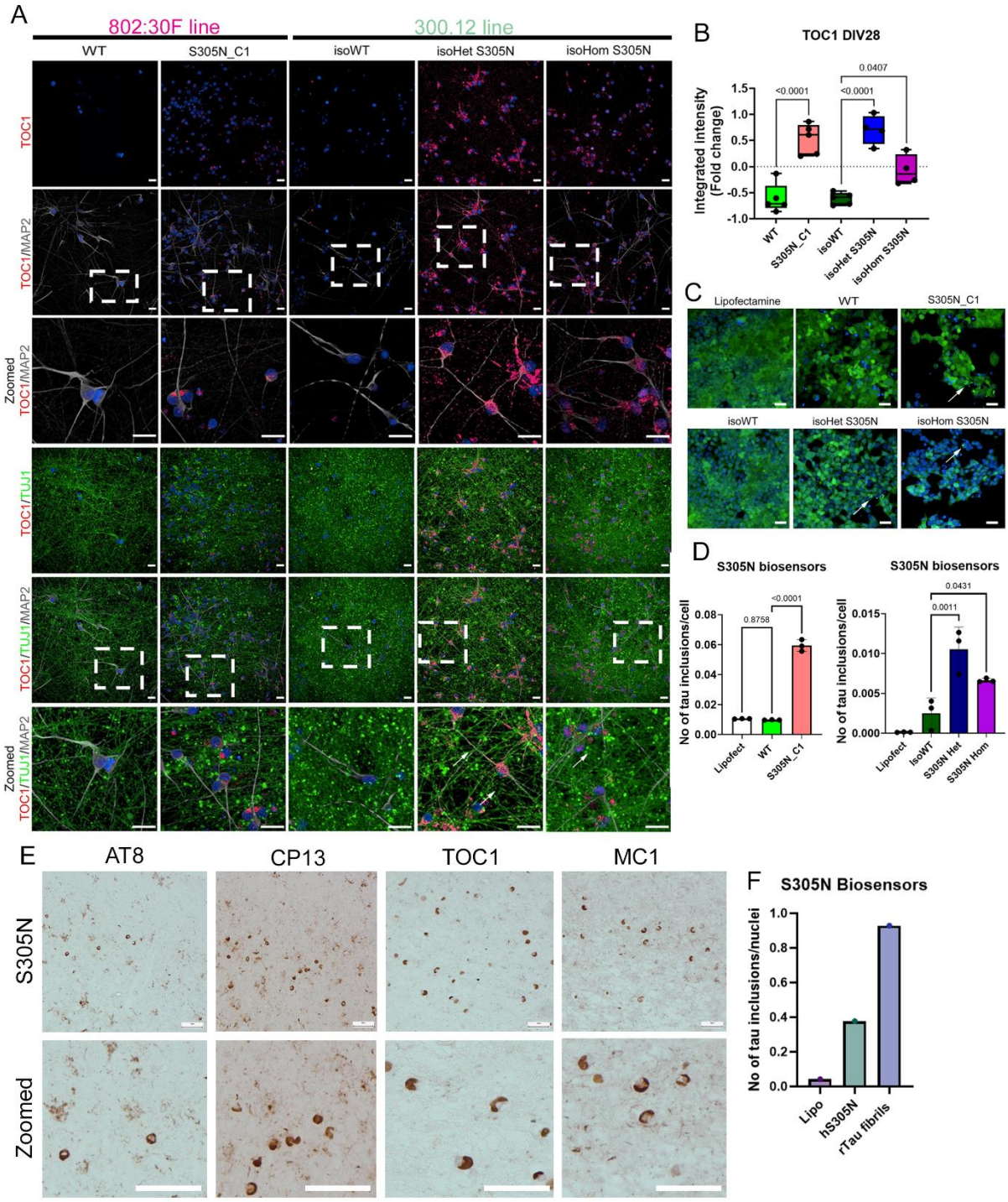
A
802:30F line
300.12 line
WT
S305N_C1
isoWT
isoHet S305N
isoHom S305N
TOC1
TOC1/MAP2
Zoomed TOC1/MAP2
TOC1/TUJ1
TOC1/TUJ1/MAP2
Zoomed TOC1/TUJ1/MAP2
B
TOC1 DIV28
Integrated intensity (Fold change)
<0.0001
<0.0001
0.0407
C
Lipofectamine
WT
S305N_C1
isoWT
isoHet S305N
isoHom S305N
D
S305N biosensors
No of tau inclusions/cell
0.8758
<0.0001
Lipofect
WT
S305N_C1
S305N biosensors
0.0011
0.0431
Lipofect
IsoWT
S305N Het
S305N Hom
E
AT8
CP13
TOC1
MC1
S305N
Zoomed
F
S305N Biosensors
No of tau inclusions/nuclei
Lipo
hS305N
rTau fibrils

Figure 5

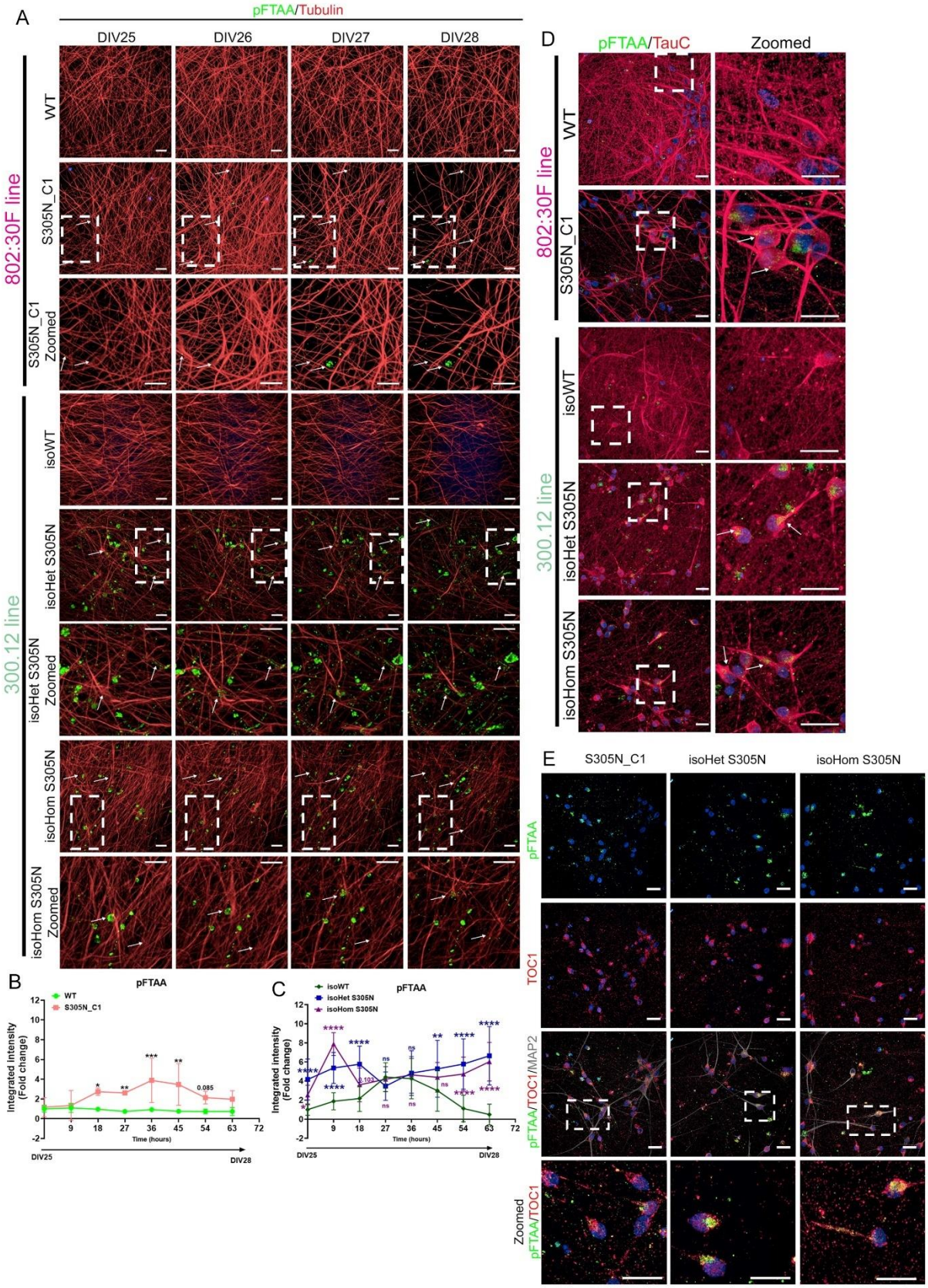
A
pFTAA/Tubulin
DIV25
DIV26
DIV27
DIV28
802:30F line
WT
S305N_C1
S305N_C1 Zoomed
300.12 line
isoWT
isoHet S305N
isoHet S305N Zoomed
isoHom S305N
isoHom S305N Zoomed
B
pFTAA
WT
S305N_C1
Integrated Intensity (Fold change)
Time (hours)
DIV25
DIV28
C
pFTAA
isoWT
isoHet S305N
isoHom S305N
Integrated Intensity (Fold change)
Time (hours)
DIV25
DIV28
D
pFTAA/TauC
Zoomed
802:30F line
WT
S305N_C1
300.12 line
isoWT
isoHet S305N
isoHom S305N
E
S305N_C1
isoHet S305N
isoHom S305N
pFTAA
TOC1
pFTAA/TOC1/MAP2
Zoomed
pFTAA/TOC1

Figure 6

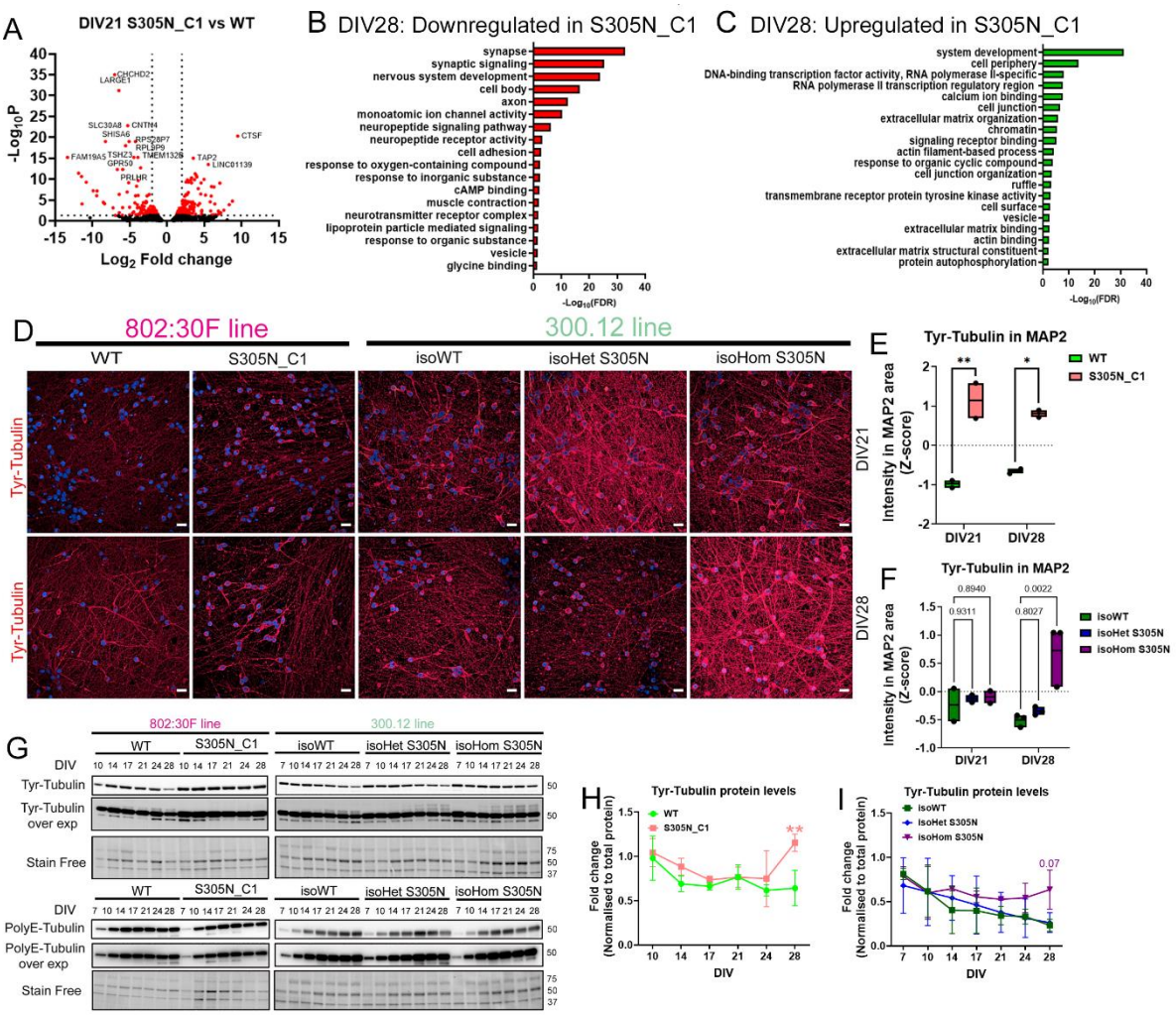
A
DIV21 S305N_C1 vs WT
-Log10P
Log2 Fold change
CHCHD2
LARGE1
SLC30A8
CNTN4
SHISA6
RPS28P7
RPL8P6
FAM19A5
TSHZ3
TMEM132B
GPR50
PRLHR
CTSF
TAP2
LINC01139
B DIV28: Downregulated in S305N_C1
synapse
synaptic signaling
nervous system development
cell body
axon
monoatomic ion channel activity
neuropeptide signaling pathway
neuropeptide receptor activity
cell adhesion
response to oxygen-containing compound
response to inorganic substance
cAMP binding
muscle contraction
neurotransmitter receptor complex
lipoprotein particle mediated signaling
response to organic substance
vesicle
glycine binding
-Log10(FDR)
C DIV28: Upregulated in S305N_C1
system development
cell periphery
DNA-binding transcription factor activity, RNA polymerase II-specific
RNA polymerase II transcription regulatory region
calcium ion binding
cell junction
extracellular matrix organization
chromatin
signaling receptor binding
actin filament-based process
response to organic cyclic compound
cell junction organization
ruffle
transmembrane receptor protein tyrosine kinase activity
cell surface
vesicle
extracellular matrix binding
actin binding
extracellular matrix structural constituent
protein autophosphorylation
-Log10(FDR)
D
802:30F line
300.12 line
WT
S305N_C1
isoWT
isoHet S305N
isoHom S305N
Tyr-Tubulin
Tyr-Tubulin
DIV21
DIV28
E
Tyr-Tubulin in MAP2
Intensity in MAP2 area (Z-score)
WT
S305N_C1
DIV21
DIV28
F
Tyr-Tubulin in MAP2
0.8940
0.0022
0.9311
0.8027
isoWT
isoHet S305N
isoHom S305N
Intensity in MAP2 area (Z-score)
DIV21
DIV28
G
802:30F line
300.12 line
WT
S305N_C1
isoWT
isoHet S305N
isoHom S305N
DIV
Tyr-Tubulin
Tyr-Tubulin over exp
Stain Free
PolyE-Tubulin
PolyE-Tubulin over exp
H
Tyr-Tubulin protein levels
WT
S305N_C1
Fold change (Normalised to total protein)
DIV
I
Tyr-Tubulin protein levels
isoWT
isoHet S305N
isoHom S305N
0.07
Fold change (Normalised to total protein)
DIV

Figure 7

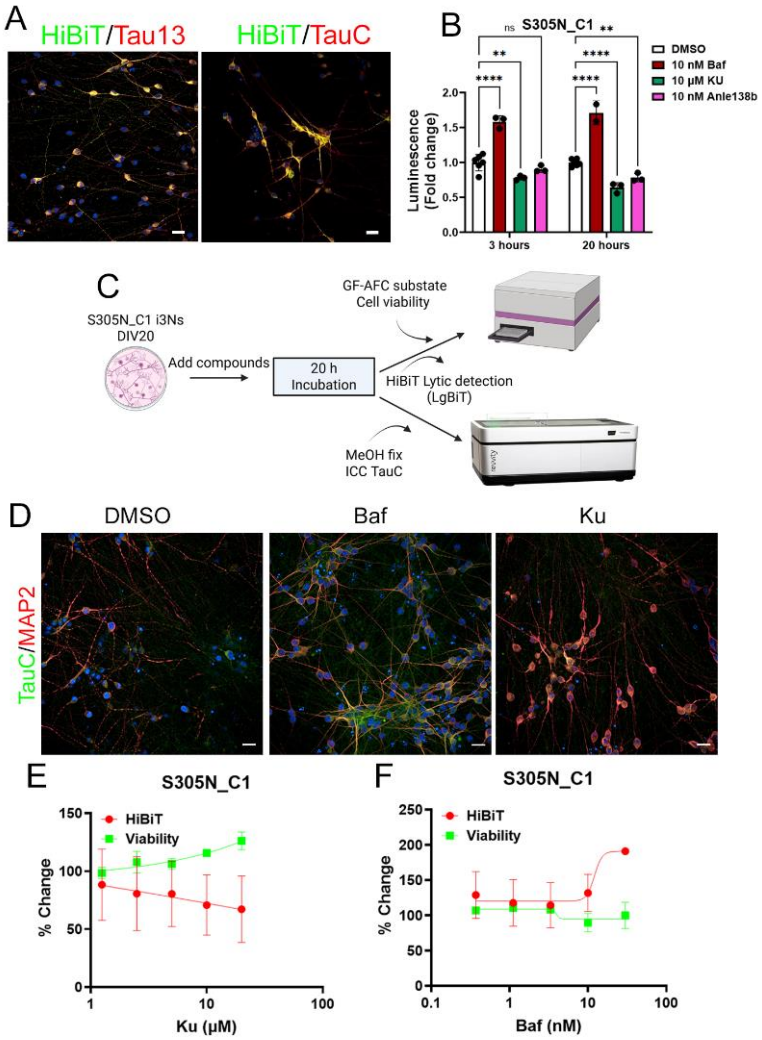
A
HiBiT/Tau13
HiBiT/TauC
B
S305N_C1
ns
**
****
DMSO
10 nM Baf
10 μM KU
10 nM Anle138b
Luminescence (Fold change)
3 hours
20 hours
C
S305N_C1 i3Ns DIV20
Add compounds
20 h Incubation
GF-AFC substate Cell viability
HiBiT Lytic detection (LgBiT)
MeOH fix ICC TauC
D
DMSO
Baf
Ku
TauC/MAP2
E
S305N_C1
HiBiT
Viability
% Change
Ku (μM)
F
S305N_C1
HiBiT
Viability
% Change
Baf (nM)

Figure 8

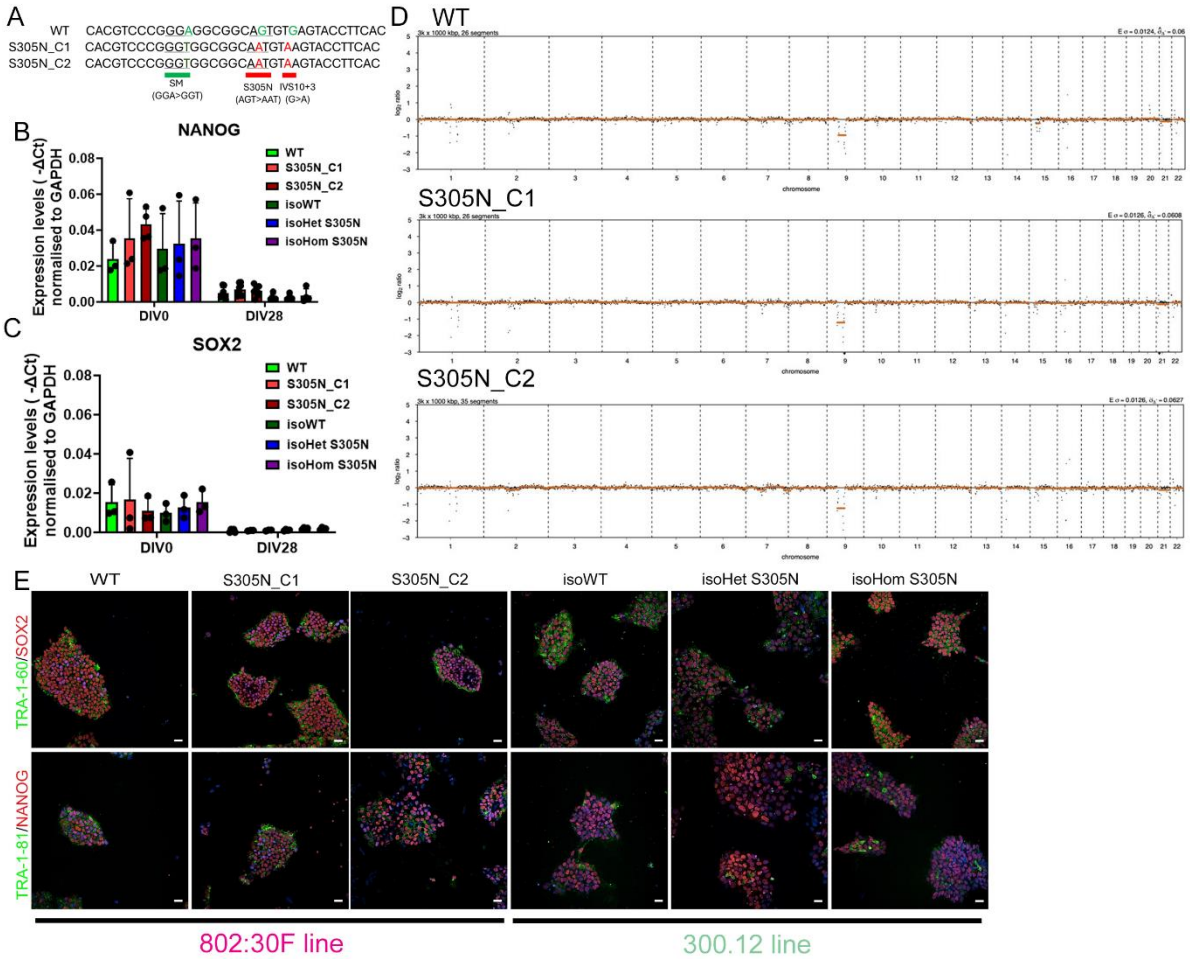
A
WT CACGTCCCGGGAGGCGGCAGTGTGAGTACCTTCAC
S305N_C1 CACGTCCCGGGTGGCGGCAATGTAAGTACCTTCAC
S305N_C2 CACGTCCCGGGTGGCGGCAATGTAAGTACCTTCAC
SM (GGA>GGT)
S305N (AGT>AAT)
IVS10+3 (G>A)
B
NANOG
Expression levels (-ΔCt) normalised to GAPDH
WT
S305N_C1
S305N_C2
isoWT
isoHet S305N
isoHom S305N
DIV0
DIV28
C
SOX2
D
WT
S305N_C1
S305N_C2
chromosome
E
WT
S305N_C1
S305N_C2
isoWT
isoHet S305N
isoHom S305N
TRA-1-60/SOX2
TRA-1-81/NANOG
802:30F line
300.12 line

Figure S1

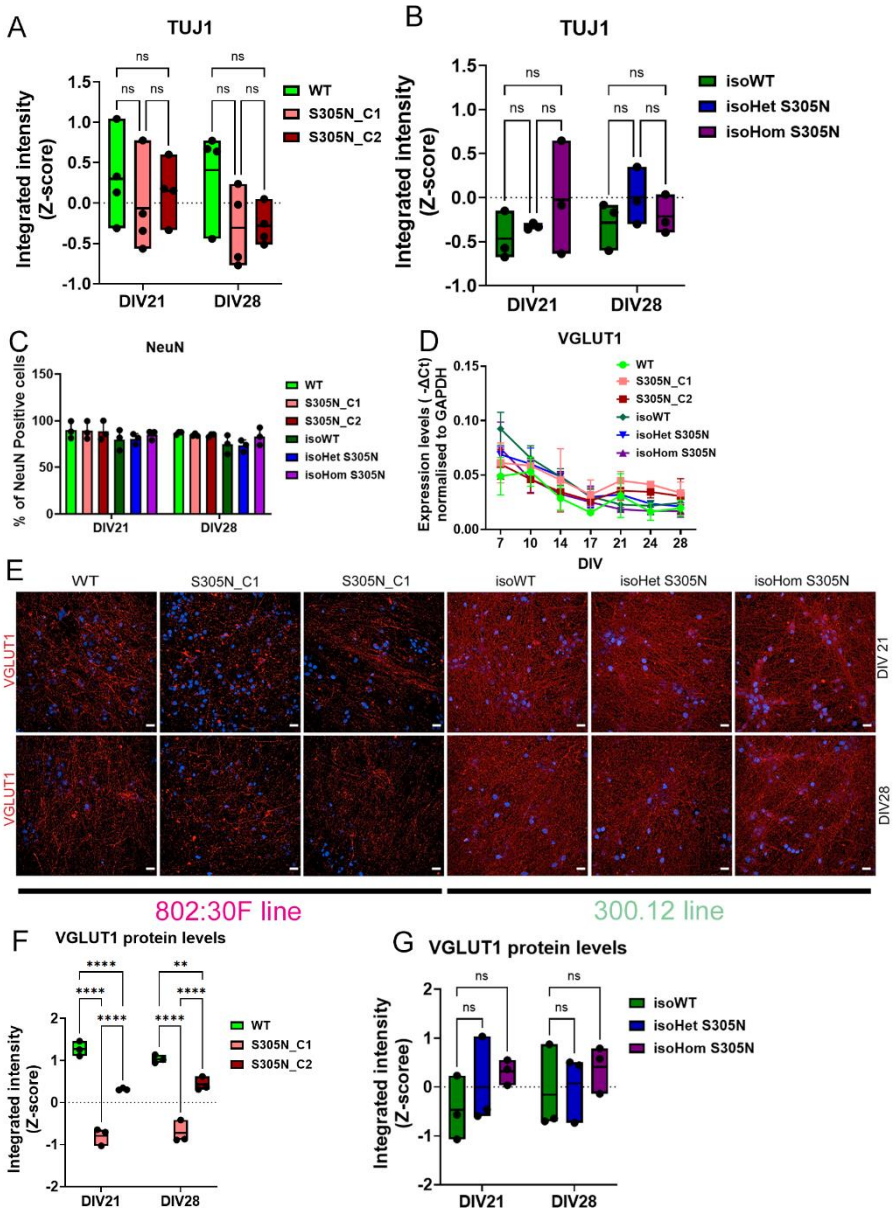
A
TUJ1
Integrated intensity (Z-score)
ns
WT
S305N_C1
S305N_C2
DIV21
DIV28
B
TUJ1
isoWT
isoHet S305N
isoHom S305N
C
NeuN
% of NeuN Positive cells
D
VGLUT1
Expression levels (-ΔCt) normalised to GAPDH
DIV
E
VGLUT1
DIV 21
DIV28
802:30F line
300.12 line
F
VGLUT1 protein levels
G
VGLUT1 protein levels

Figure S2

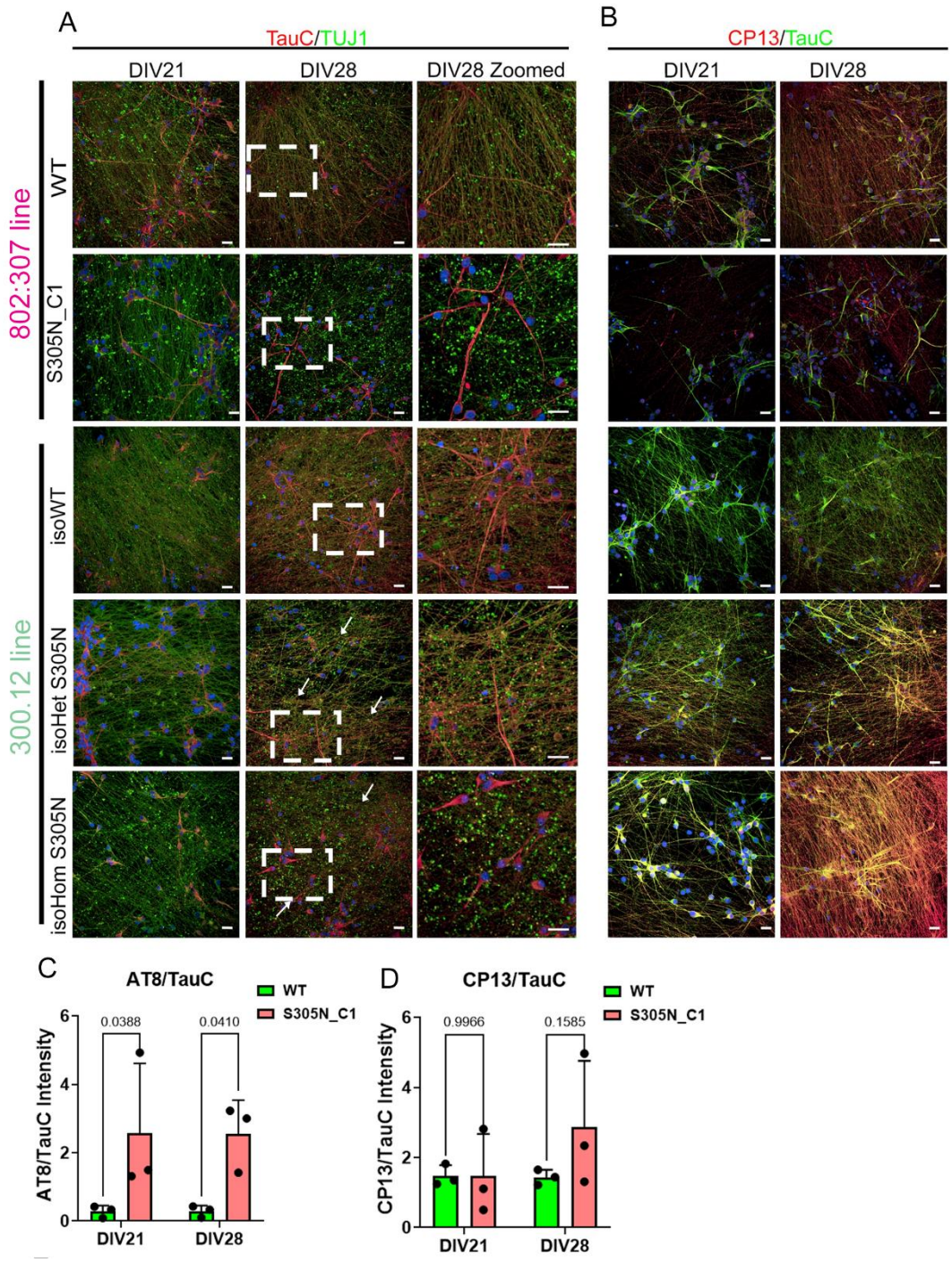
A
TauC/TUJ1
DIV21
DIV28
DIV28 Zoomed
B
CP13/TauC
DIV21
DIV28
802:307 line
WT
S305N_C1
300.12 line
isoWT
isoHet S305N
isoHom S305N
C
AT8/TauC
WT
S305N_C1
AT8/TauC Intensity
0.0388
0.0410
DIV21
DIV28
D
CP13/TauC
WT
S305N_C1
CP13/TauC Intensity
0.9966
0.1585
DIV21
DIV28

Figure S3

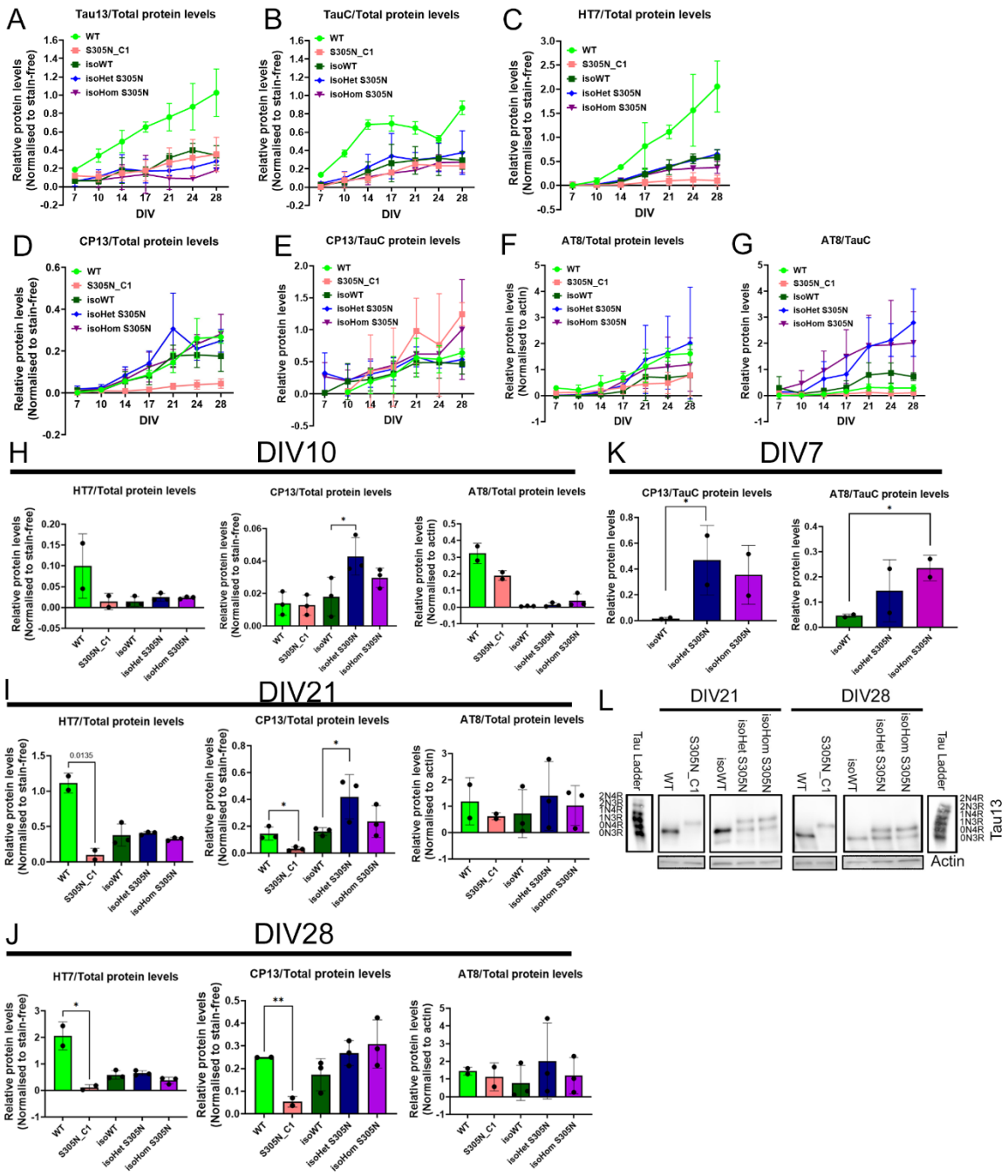
A
Tau13/Total protein levels
B
TauC/Total protein levels
C
HT7/Total protein levels
D
CP13/Total protein levels
E
CP13/TauC protein levels
F
AT8/Total protein levels
G
AT8/TauC
WT
S305N_C1
isoWT
isoHet S305N
isoHom S305N
Relative protein levels (Normalised to stain-free)
Relative protein levels (Normalised to actin)
DIV
H
DIV10
K
DIV7
I
DIV21
J
DIV28
L
DIV21
DIV28
Tau Ladder
2N4R
2N3R
1N4R
1N3R
0N4R
0N3R
Tau13
Actin

Figure S4

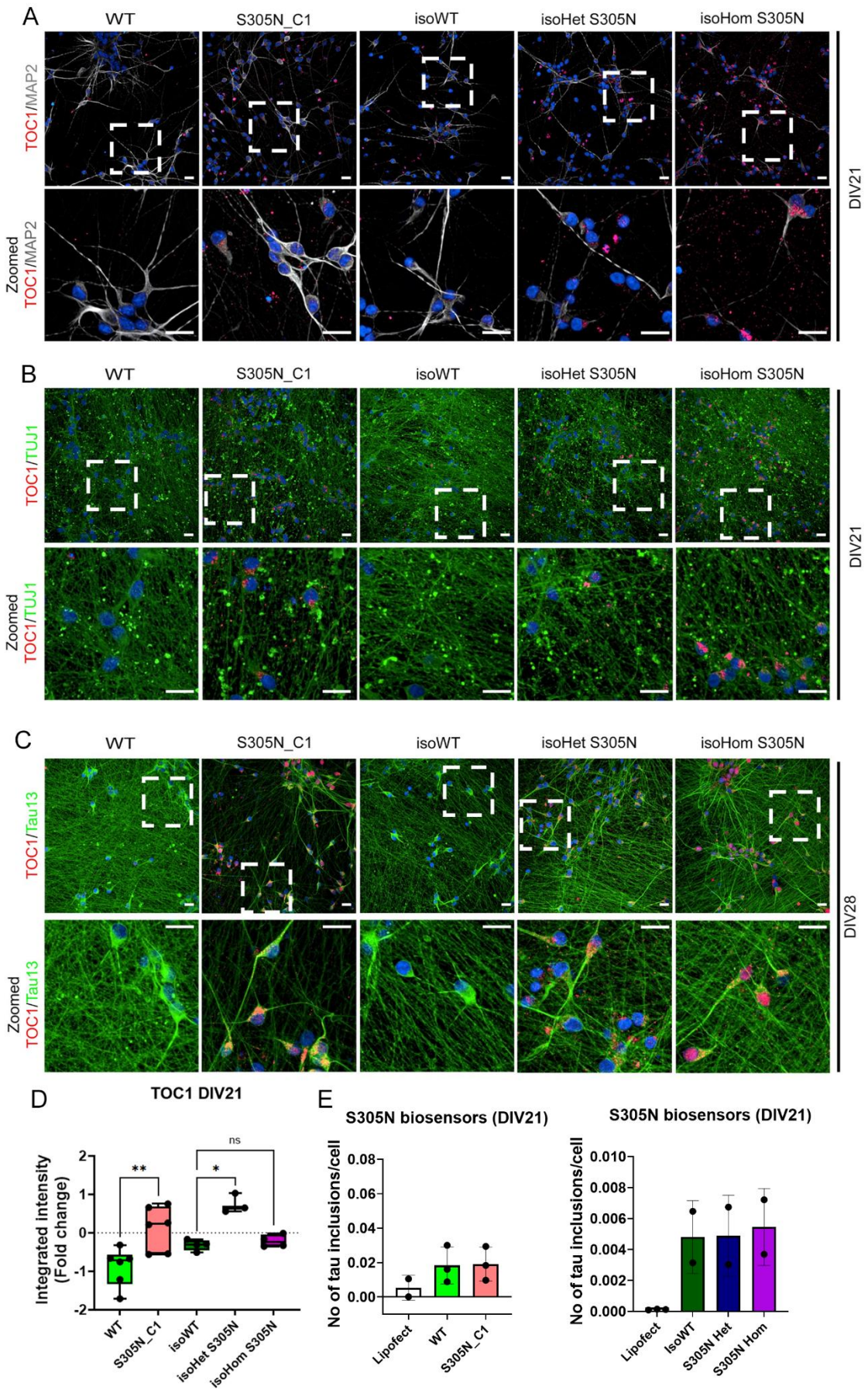
A
WT
S305N_C1
isoWT
isoHet S305N
isoHom S305N
TOC1/MAP2
Zoomed
TOC1/MAP2
DIV21
B
WT
S305N_C1
isoWT
isoHet S305N
isoHom S305N
TOC1/TUJ1
Zoomed
TOC1/TUJ1
DIV21
C
WT
S305N_C1
isoWT
isoHet S305N
isoHom S305N
TOC1/Tau13
Zoomed
TOC1/Tau13
DIV28
D
TOC1 DIV21
Integrated intensity
(Fold change)
ns
**
*
WT
S305N_C1
isoWT
isoHet S305N
isoHom S305N
E
S305N biosensors (DIV21)
No of tau inclusions/cell
Lipofect
WT
S305N_C1
S305N biosensors (DIV21)
No of tau inclusions/cell
Lipofect
IsoWT
S305N Het
S305N Hom

Figure S5

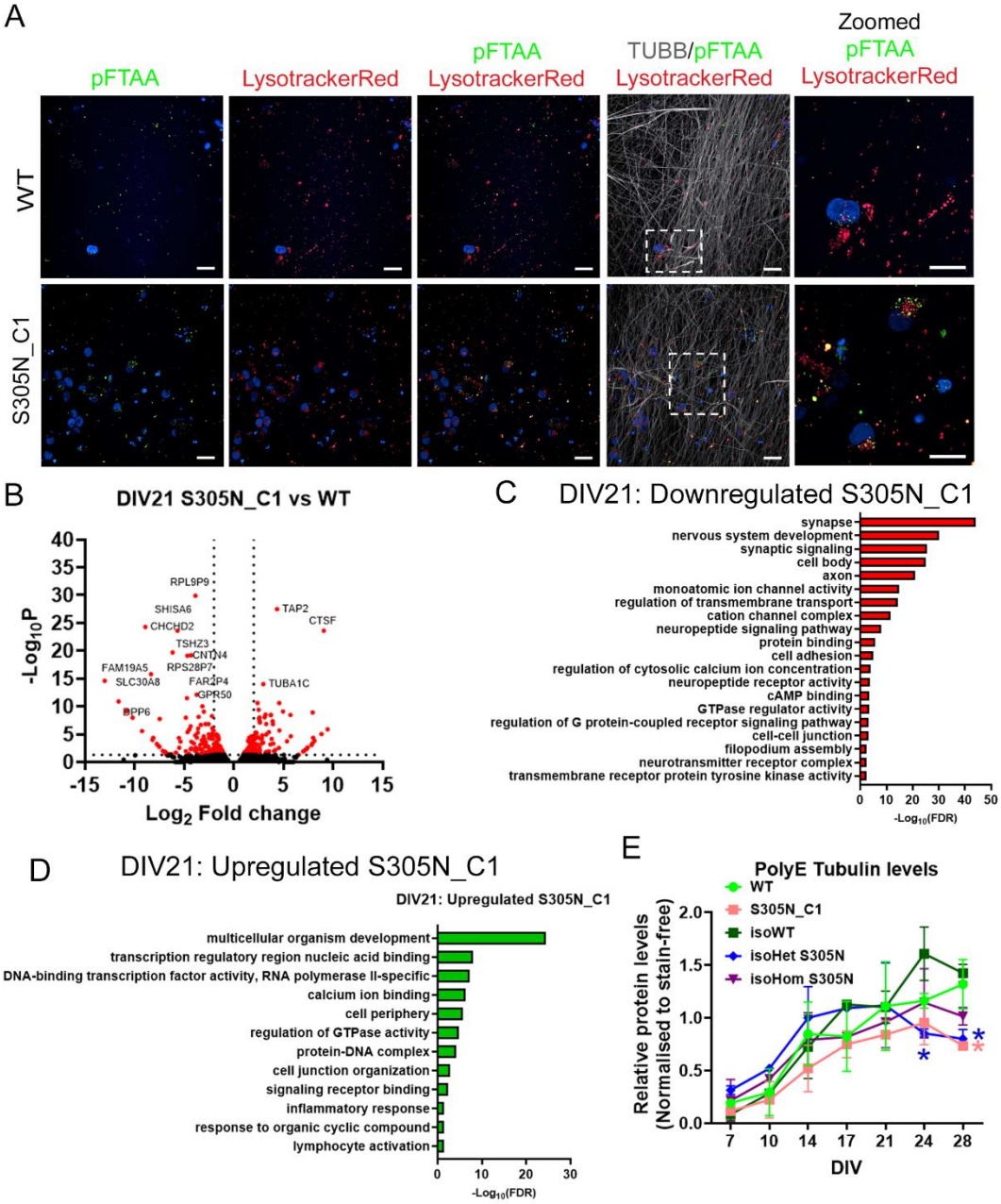
A
pFTAA
LysotrackerRed
pFTAA
LysotrackerRed
TUBB/pFTAA
LysotrackerRed
Zoomed
pFTAA
LysotrackerRed
WT
S305N_C1
B
DIV21 S305N_C1 vs WT
-Log10P
Log2 Fold change
RPL9P9
SHISA6
CHCHD2
TSHZ3
CNTN4
RPS28P7
FAM19A5
SLC30A8
FAR2P4
GPR50
BPP6
TAP2
CTSF
TUBA1C
C
DIV21: Downregulated S305N_C1
synapse
nervous system development
synaptic signaling
cell body
axon
monoatomic ion channel activity
regulation of transmembrane transport
cation channel complex
neuropeptide signaling pathway
protein binding
cell adhesion
regulation of cytosolic calcium ion concentration
neuropeptide receptor activity
cAMP binding
GTPase regulator activity
regulation of G protein-coupled receptor signaling pathway
cell-cell junction
filopodium assembly
neurotransmitter receptor complex
transmembrane receptor protein tyrosine kinase activity
-Log10(FDR)
D
DIV21: Upregulated S305N_C1
DIV21: Upregulated S305N_C1
multicellular organism development
transcription regulatory region nucleic acid binding
DNA-binding transcription factor activity, RNA polymerase II-specific
calcium ion binding
cell periphery
regulation of GTPase activity
protein-DNA complex
cell junction organization
signaling receptor binding
inflammatory response
response to organic cyclic compound
lymphocyte activation
-Log10(FDR)
E
PolyE Tubulin levels
WT
S305N_C1
isoWT
isoHet S305N
isoHom S305N
Relative protein levels
(Normalised to stain-free)
DIV

Figure S6

Table 1

	Time	DIV21			DIV28		
	Cell line	**S305N_C1**	**isoHet S305N**	**isoHom S305N**	**S305N_C1**	**isoHet S305N**	**isoHom S305N**
mRNA	4R MAPT	90%	47%	67%	90%	54%	72%
Tau aggregation	Seeding S305N biosensors	No change	No change	No change	↑↑↑	↑↑	↑
	TOC1 expression (ICC)	↑↑	↑↑	No change	↑↑↑	↑↑↑	↑↑
	pFTAA	NA	NA	NA	↑↑↑	↑↑↑↑	↑↑↑
Total Tau	Tau13 expression (ICC)	↓↓↓	No change	No change	↓↓↓	↓	No change (↓ with p=0.08)
	Tau13 expression (WB)	↓↓↓	No change	↓↓↓	↓↓↓	No change	↓↓
	HT7 expression (ICC)	↓↓↓	No change	No change	↓↓↓	No change	↑
	HT7 expression (WB)	↓↓↓↓	No change	No change	↓↓↓↓	No change	No change
	TauC expression (ICC)	↓↓↓	No change	No change	↓↓↓	No change	No change
	TauC expression (WB)	↓↓↓	No change	No change	↓↓↓	No change	No change
Phosphorylated tau	AT8 expression (ICC)	↑	↑	↑	No change	↑	↑↑
	AT8 expression (WB)[1]	No change	Variable (↑↑)	Variable (↑)	No change	Variable (↑↑)	Variable (↑)
	CP13 expression (ICC)	↓↓↓	↑	↑↑	↓↓↓	↑↑	↑↑
	CP13 expression (WB)[1]	↓↓↓	↑	No change	↓↓↓	Variable (↑)	Variable (↑)
	AT100 expression (ICC)	↓	No change	↑↑	↑	↑↑	↑
Hyperphosphorylated tau[2]	AT8/TauC (ICC)	↑↑↑↑	NA	NA	↑↑↑↑	NA	NA
	AT8/TauC (WB)[2]	No change	Variable (↑↑)	↑↑	No change	↑↑↑↑	↑↑↑
	CP13/TauC (ICC)	No change	NA	NA	Variable (↑↑)	NA	NA
	CP13/TauC (WB)[2]	No change (trend ↑)	No change (trend ↑)	No change	↑↑	No change (trend ↑)	↑↑